

The Geometric Basis of Epithelial Convergent Extension

Fridtjof Brauns^{*†1}, Nikolas H. Claussen^{*2}, Eric F. Wieschaus³, and Boris I. Shraiman^{†1,2}

¹*Kavli Institute for Theoretical Physics, University of California Santa Barbara, Santa Barbara, California 93106, USA*

²*Department of Physics, University of California Santa Barbara, Santa Barbara, California 93106, USA*

³*Department of Molecular Biology, Princeton University, Princeton, NJ, USA;
The Lewis-Sigler Institute for Integrative Genomics, Princeton University, Princeton, NJ, USA*

Abstract

Shape changes of epithelia during animal development, such as convergent extension, are achieved through concerted mechanical activity of individual cells. While much is known about the corresponding large scale tissue flow and its genetic drivers, key open questions regard the cell-scale mechanics, e.g. internal vs external driving forces, and coordination, e.g. bottom-up self-organization vs top-down genetic instruction. To address these questions, we develop a quantitative, model-based analysis framework to relate cell geometry to local tension in recently obtained timelapse imaging data of gastrulating *Drosophila* embryos. This analysis provides a systematic decomposition of cell shape changes and T1–rearrangements into internally driven, active, and externally driven, passive, contributions. Specifically, we find evidence that germ band extension is driven by active T1 processes that self-organize through positive feedback acting on tensions. More generally, our findings suggest that epithelial convergent extension results from controlled transformation of internal force balance geometry which we quantify with a novel quantification tool for local tension configurations.

Keywords: tissue mechanics, convergent extension, active and passive cell intercalation, self-organization

^{*}FB and NC contributed equally to this work.

[†]Correspondence to: fbrauns@kitp.ucsb.edu and shraiman@kitp.ucsb.edu

Introduction

Tissue elongation is one of the basic processes of morphogenesis. Tissues can elongate by oriented cell divisions and growth [1, 2], or via local rearrangements of cells. The latter happens during “convergent extension”—a common motif of early development and organogenesis in many organisms—where tissue elongates along one axis while contracting along the perpendicular direction [3]. Convergent extension also exemplifies the important role of cell and tissue mechanics in morphogenetic processes, which must be studied alongside developmental genetics and signaling. Mechanics is what directly determines physical shape, and also plays a key regulatory role further upstream by facilitating self-organized mechanical pattern formation [4, 5], in diverse systems such as feather primordia [6], the amniote primitive streak [7], and hydra body axis formation [8]. Convergent extension is often conceptualized on the continuum scale, where the morphogenetic process resembles a shear flow [9, 10]. The key challenge is to relate the large scale flow of tissue to its behavior on the scale of cells, where the active, local forces that drive the flow are generated and controlled.

Intercellular adhesion effectively links the cytoskeletons of neighboring cells, so that a two dimensional epithelial sheet constitutes a transcellular mechanical network put under tension by myosin motors. This internal tension is revealed by laser ablation of cell interfaces, which causes rapid recoil [11]. The capacity of epithelial tissue to support tension makes it markedly different from passive fluids [12]. How does one reconcile the solid-like capacity of an epithelial monolayer to support tension (as well as shear stress) with its ability to change shape and rearrange internally like a fluid? By analysing empirical data on the dynamics of cells during tissue remodelling, we shall arrive at a model of morphogenetic flow as adiabatic deformation of cell array geometry controlled by the feedback-driven changes in the internal state of tension.

One of the best-established models of morphogenetic mechanics is provided by the *Drosophila* embryo, which is ideal for live imaging and offers an extensive set of genetic tools [13]. Progress in live imaging and computational image analysis has produced remarkably quantitative data [14, 15]. In this work, we will take advantage of previously published data [15] which we will reanalyze and use as test-bed for theory development. Figure 1 recapitulates the basic quantitative features of germ band elongation (GBE) during *Drosophila* embryogenesis based on the light-sheet imaging data from [15] which, thanks to computational image processing (surface extraction [16], cell segmentation and tracking [15]), provides a global picture of tissue dynamics with cellular resolution. During *Drosophila* gastrulation, the embryonic blastoderm (an epithelial monolayer of about 6000 cells on the surface of the embryo) undergoes dramatic deformation that changes tissue topology and gives rise to the three germ layers [17]. Gastrulation starts (see Fig. 1A) with the formation of the Ventral Furrow (VF) which initiates the internalization of mesoderm, followed immediately by Germ Band Extension (GBE), which involves convergent extension of the lateral ectoderm (or germ band) and the flow of tissue from the ventral onto the dorsal side of the embryo [18–20] (see Movie 1). GBE has been extensively studied, leading to the identification of relevant developmental patterning genes [18–21]. Live imaging has also uncovered the pertinent cell behavior, namely intercalation of neighboring cells in the lateral ectoderm [21–23]. The elementary process of cell rearrangement is called a T1 transition. It involves a quartet of cells where two cells lose contact and the two other cells gain contact (see Fig. 1B, bottom). The role of intercalations is highlighted by a “tissue tectonics” [24] analysis, which decomposes the tissue strain rate into cell-level contributions: cell-shape deformation and cell rearrangement (see Fig. 1B and Fig. S1). During VF invagination, cells in the lateral ectoderm are stretched along the DV axis with little rearrangement (Fig. S1A) Subsequently, during GBE, the lateral ectoderm (i.e. the germ band) extends (Fig. 1D) by cell rearrangements with very little cell elongation (Fig. 1C, bottom; and Fig. S1B and D). By contrast, the dorsal tissue (which will become

the so amnioserosa) deforms in the opposite direction as the germ band, by a combination of cell shape changes and rearrangements (Fig. 1C, top; and Fig. S1C). Overall, we find that the majority of cell rearrangements happen via T1s (Fig. 1E and E') with only a small number of “rosettes” (which involve more than 4-cells transiently sharing a vertex) being formed. This is consistent with the high degree of spatial coordination of rearrangements that is apparent in the lateral ectoderm (Fig. 1C, bottom).

Intercalations are associated with localized activity of the force generating protein non-muscle myosin II [20, 22, 23] (henceforth, “myosin”). Myosin recruitment depends on the expression of key developmental genes [19, 20, 22, 25], and, in addition, is subject to positive and negative mechanical feedback that depends on the stress [26, 27] and the rate of strain (rate of cell deformation) [28]. Despite considerable understanding of the genetic and cell-biological components involved in GBE, the relative roles of the genetic pre-pattern versus mechanical feedback-driven “self-organization” of myosin activity are still not clear. Similarly, despite rich experimental data and great biological interest, no consensus has emerged regarding the cell-level mechanics of GBE [24, 26, 29–31]. Key questions remain open: How is myosin dynamics controlled on a cellular level? How are intercalations driven mechanically [29, 32]? What is the relative strength of locally generated forces vs pulling by adjacent tissues? How is active force generation orchestrated across cells to create a coherent global morphogenetic flow? What sets the total amount of tissue elongation? These questions call for a coherent theoretical framework that allows interpreting and reconciling existing experimental findings.

The rich dataset shown in Fig. 1 exposes a wealth of information about the mechanical behavior of cells and thus allows us to address these problems. Our approach is based on the assumption of force balance of stresses concentrated in the cell cortices. Cortical force balance provides a direct link between mechanics and geometry: It allows inference of tensions from the angles at the vertices where interfaces meet [33–35], which we utilize to identify from images the stereotyped local geometry and tension dynamics associated with internally driven (active) and externally driven (passive) cell rearrangements (T1s). We will use these insights to formulate a model for an actively intercalating cell quartet where cortical tensions dynamically self-organize via a positive feedback mechanism while remaining in force balance. This model reproduces the experimentally observed dynamics on the level of cell quartets and forms the basis for a predictive tissue-scale model that is formulated in a companion paper [36]. Finally, we address how cellular behaviors (shape changes and intercalations) are coordinated across the tissue to generate coherent tissue flow. We will show that coordination of active T1 events among neighboring cells involves a characteristic pattern of cortical tensions which we quantify by introducing the “Local Tension Configuration” (LTC) order parameter. In the companion paper [36], we employ this order parameter to quantitatively compare tissue-scale simulations with experimental data on the cell scale.

Results

Force balance and cell geometry in an epithelial monolayer

We begin by laying out the assumptions and concepts that underlie our framework. Epithelial tissues are under internally generated tension, which is revealed by recoil in response to laser ablation. The timescale of this recoil (~ 10 s) on the scale of cells is at least 10-fold faster than the timescale of local tissue flow [37, 38], so that the tissue can be regarded as being in approximate mechanical equilibrium. This suggests that the apparent tissue flow can be understood in terms of adiabatic remodelling of a quasistatic force balance network [35]. This view contrasts with regular fluid flow, where externally or internally generated forces are balanced by viscosity or substrate friction.

We further assume that mechanical stress in the epithelium is primarily carried

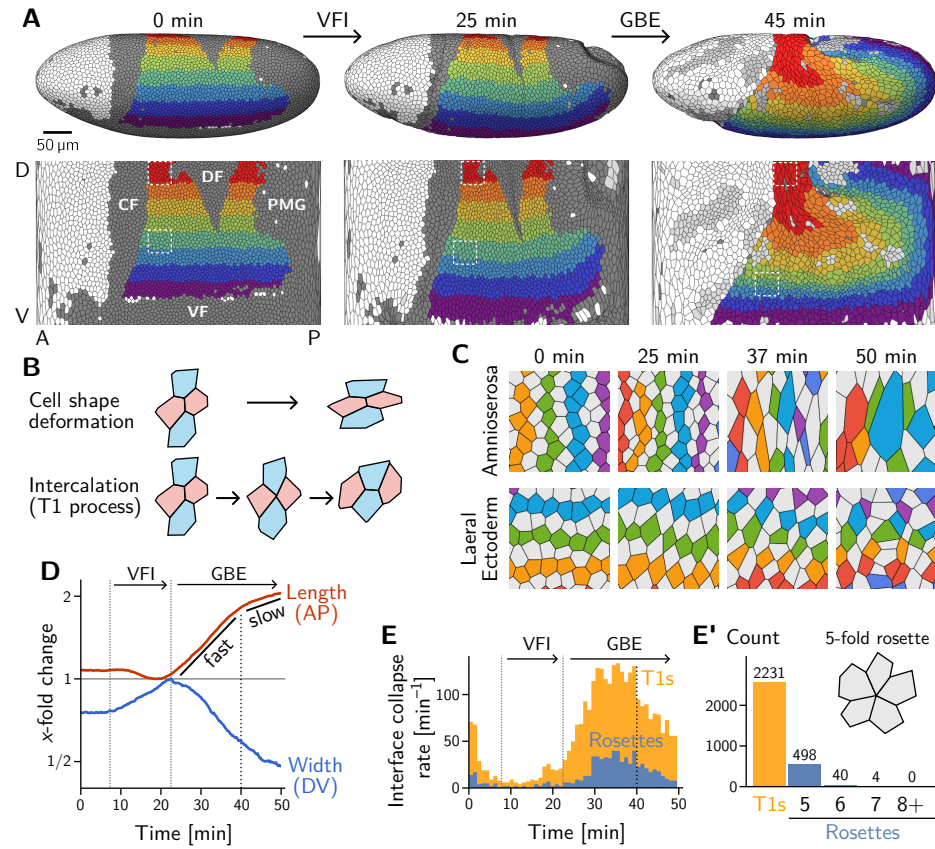


Figure 1: Light sheet imaging, segmentation, and tracking [15] provides a global picture of the cell level contributions to tissue flow (“tissue tectonics” [24]) during *Drosophila* gastrulation. **A Segmented and tracked cells on the ellipsoidal surface of the early *Drosophila* embryo in 3D (top) and projected into the plane (bottom) using a cartographic projection [16]; imaging, segmentation and tracking data from Ref. [15]. Trunk cells are colored in bands along the DV axis to illustrate the major tissue deformations during early development of *Drosophila*: ventral furrow invagination (VFI, 25 min) and germ band extension (GBE, 45 min). The purple to green regions constitute the lateral ectoderm (germ band) which contracts along the DV axis and extends along the AP axis. The posterior part of the germ band moves over the pole as it extends. The red and orange regions constitute the amnioserosa, which contracts along the AP axis and extends along the DV axis. Cells that are internalized in folds are shaded in dark gray (CF: Cephalic furrow; DF: Dorsal folds; VF: Ventral furrow; PMG: posterior midgut). Only one side of the left-right symmetric embryo is shown but both sides were analyzed throughout the manuscript. **B** Tissue deformation is the sum of cell shape changes (top) and cell rearrangements (bottom). The elementary cell rearrangement is a T1 transition in a quartet of cells. The interface between the red cells collapses, giving rise to a transient four-fold vertex configuration (center). The four-fold vertex then resolves to form a new interface between the blue cells. **C** Colored, tracked cells illustrate the cell rearrangements and shape changes in the amnioserosa (top) and lateral ectoderm (bottom). While amnioserosa cells show large deformations and little coordination in their rearrangement, cell intercalations in the lateral ectoderm appear highly choreographed. (ROI size $40 \times 40 \mu\text{m}^2$.) **D** Convergence and extension of the lateral ectoderm (x -fold change defined relative to the minimum length and maximum width respectively). During VFI, the lateral ectoderm is stretched along DV axis and slightly contracts along the AP axis. GBE has an initial fast phase before slowing down at around 40 min. **E** and **E'** Rate of interface collapses serves as a measure for the cell intercalation rate. During VFI, there are few intercalations. During GBE, the majority of intercalations are T1 transitions, while rosettes, rearrangements involving more than four cells, contribute significantly less to tissue deformation (E'). At 40 min, there is a noticeable drop in the T1 rate, marking the transition to the slow phase of GBE. Intercalation events before $t = 12$ min were excluded from the subsequent analysis.**

by the adherens-junctional cytoskeleton, which resides on cell interfaces. This is supported by the observation that cell-cell interfaces in the *Drosophila* blastoderm are mostly straight. Cells are attached to their neighbors via adherens junctions that are linked to the junctional cytoskeleton in each cell (Fig. 2A) [39]. The myosin motors exert a contractile force on the actin fibers and thereby keep the cortex under active tension (T), which we refer to as “cortical tension” [40]. Together, the adherens junctions define a tissue-wide mechanical structure, capable of (i) generating locally controlled internal tension and (ii) adaptively remodelling its architecture. The *Drosophila* blastoderm lies on top of a fluid yolk [41] which exerts negligible drag forces on tissue motion on the surface [42], suggesting that all forces are balanced within the epithelial layer.

Concentration of tension in interfaces tightly links force balance with the readily observable geometry of cell-cell interfaces. Force balance requires that the forces \mathbf{T}_{ab} exerted by the cortical tensions sum to zero at each vertex where three (or more) interfaces meet. (Here, the indices a, b label the two cells that meet at a interface; see Fig. 2A.) These force-balance constraints relate the *relative* tension on cell interfaces at a vertex to the angles at which the interfaces meet [33]. This link of hard-to-observe cortical tensions to the readily observable local cell geometry enables tension inference methods which have been extensively validated by computational robustness checks [34], direct comparison with measured laser ablation recoils [43] and by correlation with local myosin abundance [35].

Crucially, the link between force balance and the geometry of the cell tessellation goes beyond inference and to the very basis of our proposed mechanism of tissue flow. Force balance implies that tension vectors meeting at a vertex sum to zero and hence form a closed triangle [12], as illustrated in Fig. 3B. The angles of this triangle are complementary to the corresponding angles at which the interfaces meet. (This becomes evident by rotating each triangle edge by 90°. Two angles are complimentary if they sum to 180°) As adjacent vertices share an interface, the corresponding tension triangles must share an edge: the tension triangles form a triangulation, i.e. fit together to form a tiling of the plane. The triangulation is dual to the cell tessellation: For each cell, there is a corresponding vertex in the tension triangulation (Fig. 3B'). It reflects the fact that the force-balance conditions at neighboring vertices are not independent because they share the interface that connects them. (Dual force tilings go back to Maxwell [44] and have been applied to the statics of beam assemblies [45] and granular materials [46].) This triangulation establishes a geometric structure in tension space. Force balance requires that the angles at vertices in the physical cell tessellation are complementary to those in the tension triangulation. This intimately links tension space and epithelial geometry in real space. Myosin-driven local changes in tension change the shapes of tension-space triangles and hence remodel the tension triangulation. The induced changes in the geometry of the cell tessellation drive both the local rearrangement of cells and the global tissue flow. The remainder of the Results section will provide quantitative data analysis and modelling that will work out the above ideas and their implications.

Cell scale analysis

By applying local tension inference to each interface – using the angles it forms with its four neighboring interfaces – we can map out the relative tensions in the tissue, as shown in Fig. 2C and C'. Initially, relative tensions are close to unity throughout the embryo, since the cell tessellation is approximately a hexagonal lattice, with vertex angles close to 120°. As gastrulation progresses, the cortical tensions change and one starts to see characteristic differences between the dorsal ectoderm (amnioserosa) and the lateral ectoderm (germ band). In the former, interfaces that contract remain under approximately constant tension while interfaces oriented parallel to the direction of tissue stretching (i.e. along the DV axis)

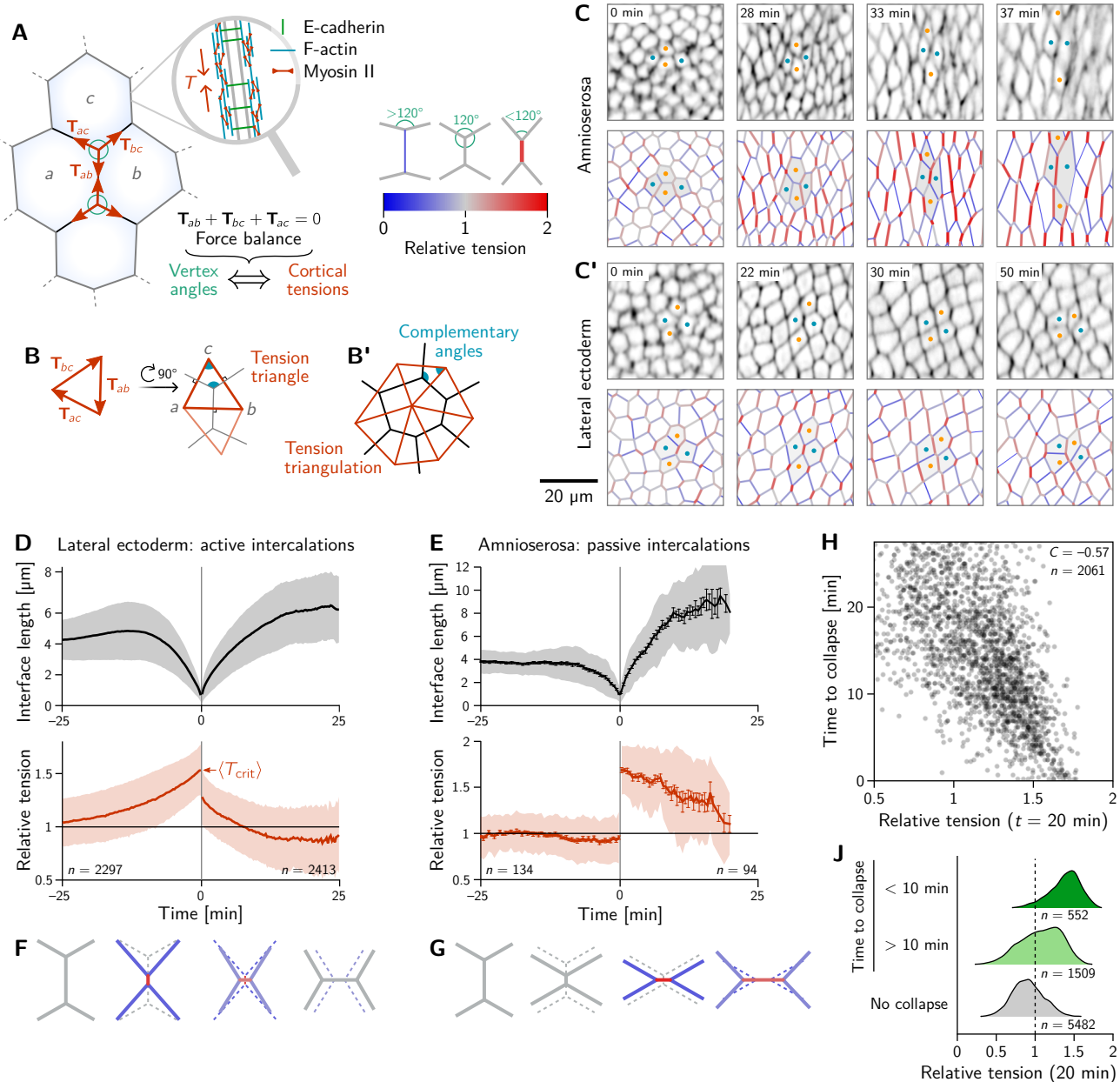


Figure 2: Inferred tension dynamics distinguishes active and passive T1s. **A** The adherens-junctional cytoskeleton maintains tension in the cortex at cell-cell interfaces via active motors (inset). In force balance, the forces T_{ab} exerted on a vertex (red arrows) must sum to zero. This allows inferring the relative cortical tensions from the angles at which the interfaces meet at a vertex (see colorbar). **B and B'** The angles in the *tension triangles* formed by the force vectors (rotated by 90°) are complementary to the interface angles at the vertex. Tension triangles corresponding to adjacent vertices share an edge and therefore fit together to form a *tension triangulation* (B'). **C and C'** Relative tensions inferred (bottom) from cell membrane images (top) in the amnioserosa (C) and in the lateral ectoderm (C'). In the lateral ectoderm, high tension interfaces contract. The regular pattern of alternating high and low tension interfaces therefore leads to coordinated T1s (cf. Fig. 1C, bottom). Blue and orange dots mark an intercalating quartet. **D and E** While active and passive T1s show similar dynamics of the length of the inner edge (top), they are markedly different in their tension dynamics (bottom). For lateral cells (D), the tension increases as the interface contracts, providing evidence that positive tension feedback actively drives the edge contraction. For dorsal cells (E), the relative tension remains constant on the contracting edge, indicating that the intercalations are passive. Tension jumps at time zero result from the relation between the angles before and after the neighbor exchange. Collapsing and emerging interfaces were tracked and analyzed separately (see SI Sec. 1.3). Bands and fences show SD and SEM respectively; the SEM in (D) is smaller than the line thickness. **F** The increasing tension of the contracting edge during an active T1 causes the angles opposite of the central interface to become increasingly acute. **G** The hallmark of passive T1s are constant cortical tensions (and thus vertex angles) before the neighbor exchange. This geometrically fixes the vertex angles after the neighbor exchange, such that the emerging edge is under high tension. **H and J** In the lateral ectoderm, relative tension predicts time until a interface collapses (H) and high relative tension predicts which interfaces collapse (J); see Fig. S4 for analogous plots for the amnioserosa where no such correlation is observed. Relative tensions were averaged from minute 20 to 21 (over four timepoints), i.e. at the end of VFI (cf. Fig. 1E).

extend and are under increasing tension (Fig. 2C). A very different picture emerges in the lateral ectoderm, where one observes an alternating pattern of high and low tensions before intercalations start (22 min). The high tension interfaces contract, leading to coordinated T1 transitions (30 min, cf. Fig. 2C' and Movie 2). As GBE transitions from the fast phase to the slow phase at around 40 min, the pattern of tensions becomes more disordered. We will return to the pattern of local tension configurations below in the discussion of tissue scale dynamics.

The differences in the patterns of inferred tension in the amnioserosa compared to the lateral ectoderm suggest very distinct mechanisms for cell intercalations in these two tissue regions, matching the fact that their levels of cortical myosin are very different (high in the lateral ectoderm, low in the amnioserosa [10]). In the following, we first focus on intercalating cell quartets to quantitatively analyze these different mechanisms. A quantitative understanding of the cell-scale dynamics will then form the basis for bridging to the tissue scale.

Relative tension dynamics distinguishes active and passive intercalations

We identify all cell quartets which undergo neighbor exchanges (T1 processes), calculate the length and relative tension of all collapsing and emerging interfaces and align the data to the time of the neighbor exchange [47]. Pooling the data for each of the bands of cells colored in Fig. 1A, we find two distinct scenarios for ventro-lateral quartets and dorsal quartets (Fig. 2D and E; for a breakdown by individual bands, see Fig. S3).

The length dynamics of collapsing and extending interfaces in the amnioserosa and the lateral ectoderm is qualitatively similar (Fig. 2D and E). In the lateral ectoderm, there is a slight increase in interface length preceding contraction. This transient stretching is caused by the VF invagination that precedes GBE [28].

By contrast, the tension dynamics is markedly different between the amnioserosa and the lateral ectoderm. In the lateral ectoderm, the tension on the contracting edge grows non-linearly and reaches its maximum just before the neighbor exchange. In terms of the local cell geometry, this increasing relative tension reflects the fact that the angles facing away from the interface decrease as the interface contracts (Fig. 2F). Notably, the non-linearly increasing tension, concomitant with an accelerating rate of interface contraction, is evidence that positive tension feedback plays a role in myosin recruitment [26, 27] and is in excellent agreement with predictions from a recent model where such feedback is a key ingredient [48]. From the data shown in Fig. 2D we can read off the average relative tension threshold $\langle T_{\text{crit}} \rangle = 1.530 \pm 0.005$ for interface collapse. As we will see further below, this threshold can be predicted from simple geometric considerations.

The correlation between increasing tension and interface contraction during active T1s can be used to predict active T1s. Indeed, plotting the time to interface collapse against the relative tension for quartets in the lateral ectoderm shows a clear negative correlation (Fig. 2H). Conversely, relative tensions below 1 correlate with interfaces that never collapse (Fig. 2J).

After the neighbor exchange, the relative tension on the new interface jumps to a lower value and then continues decreasing back to 1, corresponding to vertex angles of 120° . The jump in relative tension between the collapsing and the emerging interface is a consequence of geometry: Because the angles facing away from the interface are $< 90^\circ$ before the neighbor exchange, they are necessarily $> 90^\circ$ afterwards. This implies a jump of the relative tension from $> \sqrt{2}$ to $< \sqrt{2}$.

Let us now turn to T1s in the amnioserosa. Here, the relative tension on the inner edge remains almost constant near 1 prior to the neighbor exchange, i.e. the vertex angles remain close to 120° (see Fig. 2G). As a consequence of this tension homeostasis on collapsing interfaces, there is no correlation between relative tension and the time until the interface collapses in the amnioserosa (see Fig. S4). On the new interface emerging after the neighbor exchange, tension is high and remains

constant for an extended period. Again, the tension jump across the neighbor exchange is a consequence of geometry. Just before the neighbor exchange the vertex angles are close to 120° which implies that the angles facing away from the interface are 60° after the neighbor exchange (see Fig. 2G). This corresponds to a relative tension of $\sqrt{3} \approx 1.73$ on the central interface. Just before the neighbor exchange the vertex angles are close to 120° which implies that the angles facing away from the interface are 60° after the neighbor exchange (see Fig. 2G). This corresponds to a relative tension of $\sqrt{3} \approx 1.73$ on the central interface.

A tension–isogonal decomposition quantifies active vs passive contributions to tissue deformation

Tension inference and the pooled analysis of T1 events has revealed the cortical tension dynamics on cell-cell interfaces during active and passive cell intercalations. The cortical tension behaviour is quite counter-intuitive and differs significantly between distinct spatial regions of the embryo. In particular, it is very differently from that of springs or rubber bands: the length and tension of a spring are tied to one another by a constitutive relationship. By contrast, both the length and tension of cell-cell interfaces are can change independently and are actively regulated by turnover of junctional proteins (such as actin, myosin and E-cadherin).

This raises the question how the regulation of tensions controls the cell and tissue shape. The answer to this question lies in the force balance constraint that links tension and geometry which we have previously used to inferring the tensions from the observed epithelial geometry. Recall that force balance implies that the cortical tensions form a triangulation such that the angles at vertices in the physical cell tessellation are complementary to those in the tension triangulation (Fig. 3A, left). However, force balance does not uniquely determine the cell tessellation (i.e. the positions of the cell vertices) since interface lengths may collectively change while preserving angles via so-called *isogonal* modes [12], as illustrated in Fig. 3A, right. Thanks to the relative sliding of cytoskeletal elements (e.g. due to the turnover of passive crosslinkers or walking of myosin motors), cell-cell interfaces can extend or contract under constant tension, behaving similar to a muscle rather than a spring. These considerations motivate a decomposition of the tissue deformations into two distinct contributions: deformations of the tension triangulation reflecting changing cortical tensions, and isogonal (angle-preserving) deformations (see Fig. 3B). We will call this a *tension–isogonal decomposition*. The isogonal degrees of freedom allow for tissue deformations at fixed tensions (tension homeostasis) and therefore account for cell shape deformations driven by external forces or cell-internal stresses (hydrostatic pressure, medial myosin [29, 32], stiffness of the nucleus, intermediate filaments and microtubules [49–51]). It is important to keep in mind that this association of isogonal deformations with non-junctional (e.g. cell-elastic or external) stresses is based on the assumption that active cortical stresses are the dominant source of stress in the tissue (separation of scales).

Implicitly, the tension–isogonal decomposition uses the fact that we can construct a reference state for the cell tessellation—compatible with the force balance constraints—from the tension triangulation (e.g. using a Voronoi tessellation). Isogonal deformations then transform this reference state into the physical cell tessellation. In practice, we do not need to explicitly construct the reference cell tessellation. Instead, we utilize the fact that the physical cell tessellation can be quantified by the triangulation defined by the cells’ centroids [52]. The isogonal modes are calculated as the transformations that deform the tension triangulation into the centroidal triangulation.

We first apply the tension–isogonal decomposition to intercalating quartets. For a given quartet of cells labelled $i = 1–4$, we quantify the physical shape in terms of the centroid positions \mathbf{c}_i by calculating the moment of inertia tensor (see Fig. 3C). The tension reference shape is given by the tension vectors $\hat{\mathbf{T}}_{ij}$, which are obtained from the interface angles using tension inference and are rotated by 90° relative

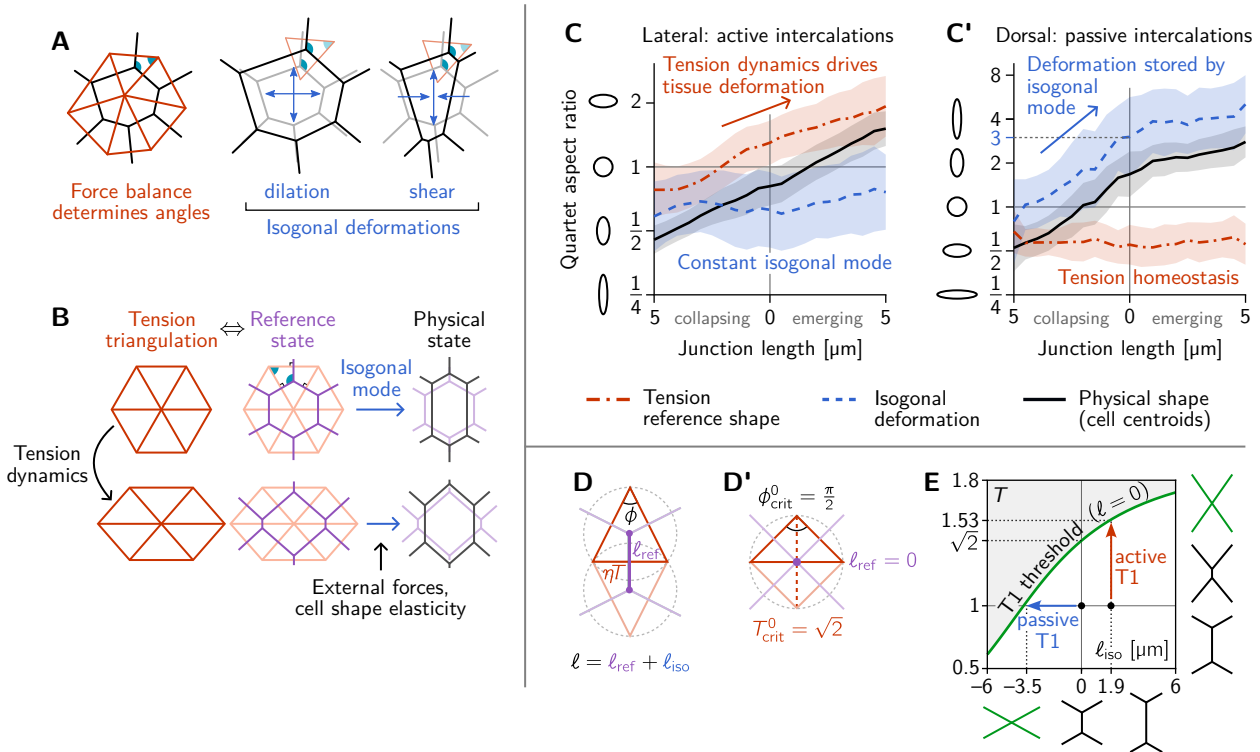


Figure 3: Tension–isogonal decomposition of epithelial geometry identifies active (tension-driven) and passive contributions to tissue deformation. **A** The angles in the tension triangulation (red) are complementary to those in the cell tessellation (black) (left). The triangulation acts as a scaffold which leaves freedom for isogonal (angle preserving) deformations which encompass both dilation (center) and shear (right). **B** Deformations of the physical cell tessellation (black, right) can be decomposed into deformations of the tension triangulation (red, left) and isogonal deformations (blue). The former reflect the dynamics of cortical tensions while the latter reflect the effect of external forces and cell shape elasticity. A reference cell tessellation (purple, e.g. a Voronoi tessellation) constructed from the tension triangulation serves as an intermediate relative to which the isogonal deformations are defined. **C and C'** Quartet shape (aspect ratio) and isogonal mode plotted against the length of the quartet’s inner interface, which serves as a pseudo-time parametrization. An aspect ratio of 1 indicates an isotropic quartet shape and no isogonal deformation, respectively. Active T_1 s (left), are driven by a deformation of the tension triangulation while the isogonal mode remains constant. Passive T_1 s (right), are driven by isogonal deformations while the shape of the tension triangulation remains constant. Bands indicate SD; SEM is smaller than the line width. **D** A symmetric pair of tension triangles is characterized by a single angle ϕ . The cell quartet’s central interface in the Voronoi reference configuration (purple) connects the centers of the triangles’ circumcircles (dashed gray circles). The general case of asymmetric triangles, characterized by two internal angles, is discussed in the companion paper [36]. **D'** The circumcircles coincide when $\phi = \phi_{\text{crit}}^0 = \pi/2$. **E** T_1 threshold for symmetric cell quartets in the T - $\Delta\ell_{\text{iso}}$ plane. Along the T_1 threshold, the physical interface length $\ell = \ell_{\text{ref}} + \Delta\ell_{\text{iso}}$ vanishes. The threshold can be reached by isogonal contraction under constant relative tension (blue arrow) or by active contraction under increasing relative tension (red arrow).

to the interfaces (see Fig. 2B). The ratios of eigenvalues of the moment-of-inertia tensors defines the shape aspect ratios, illustrated by ellipses in Fig. 3C–C'. The quartet's isogonal deformation tensor $\mathbf{I}_{\text{quartet}}$ transforms the cell centroids into the tension vertices $\eta \mathbf{I}_{\text{quartet}} \hat{\mathbf{T}}_{ij} = \mathbf{c}_i - \mathbf{c}_j$. Given $\hat{\mathbf{T}}_{ij}$ and \mathbf{c}_i , $\mathbf{I}_{\text{quartet}}$ can be obtained using least squares. The constant, global scale factor $\eta \approx 6 \mu\text{m}$ translates units from relative tensions (a.u.) to length (μm) and is fitted to minimize initial strain in the initial state. In Fig. 3C and C', we plot the quartet shape aspect ratios and the elongation factor of the isogonal deformation against the length of the quartet's inner edge, which serves as a pseudo-time parameterization of the T1 process. (Plots against real time are shown in Fig. S6B and B'.) In the lateral ectoderm, the tension-triangle deformation leads the quartet shape deformation, indicating that tension dynamics drives the intercalation (Fig. 3C). This confirms our conclusion from the relative tension analysis (Fig. 2D). The isogonal strain is approximately constant and, in fact, slightly counteracts the deformation. This is a consequence of the ventral furrow invagination which pulls on the lateral ectoderm cells and passively stretches them along the DV axis. A very different picture emerges in the passively deforming amnioserosa (Fig. 3C'). Here, the tension mode is constant—indicating tension homeostasis—while the cell quartet deformation is entirely stored in the isogonal mode. While the behaviors observed in the lateral ectoderm and in the amnioserosa represent the extreme cases, being purely tension driven (active) in the former and purely isogonal (passive) in the latter, there is continuous spectrum in between. Intermediate scenarios where both cortical tensions and external stresses contribute to tissue deformation are conceivable and can be detected and analyzed using the tension-isogonal decomposition.

Taken together, the tension-isogonal decomposition quantitatively distinguishes between active and passive intercalations. Tensions are controlled locally, while the isogonal modes accommodate external, non-local forces, such as pulling by adjacent tissue. We associate isogonal deformations with passive deformations because active stresses in the lateral ectoderm are generated at interfaces. In systems where active stresses are generated in the cell's interior, e.g. due to nuclear migration [53] or due to intracellular actin cables [54], the isogonal mode is actively controlled. Another example for this is apical constriction during VF invagination which is driven by medial myosin pulses that drive isogonal cell contractions [12].

Tension space geometry sets the threshold for interface collapse

A puzzle that has remained open so far is the threshold for interface collapse during a cell neighbor exchange. In the lateral ectoderm, where the isogonal strain is approximately constant (Fig. 3C), the neighbor exchange takes place at a critical relative tension of 1.530 ± 0.005 on average (cf. Fig. 2D). By contrast, in the amnioserosa, where T1s take place under constant tension (Fig. 2E), there is an average critical aspect ratio ~ 3 of the isogonal deformation at the point of neighbor exchange (see Fig. 3C').

We now explain these numbers in terms of the geometric tension-isogonal decomposition introduced in the previous section. We start by decomposing the length ℓ of a cell quartet's central interface into a reference length $\ell_{\text{ref}}(\{T_i\})$, determined purely in terms of the local relative tensions, and an isogonal length $\Delta\ell_{\text{iso}}$ depending on the quartet's isogonal strain:

$$\ell = \ell_{\text{ref}}(\{T_i\}) + \Delta\ell_{\text{iso}}. \quad (1)$$

A neighbor exchange takes place when ℓ shrinks to zero. From the decomposition Eq. (1) it is apparent that the interface collapse can be driven by the isogonal mode, by changes in tensions, or by a mixture of both.

Let us start with the passive T1s observed near the dorsal pole. In this case, the relative tensions are homeostatic (cf. Fig. 2E), so $\ell_{\text{ref}} \approx \langle \ell(0) \rangle \approx 3.5 \mu\text{m}$ remains constant. The neighbor exchange therefore happens when $\Delta\ell_{\text{iso}} = -\langle \ell(0) \rangle$ (see

blue arrow in Fig. 3E). By a geometric construction (Fig. S6D) one finds that the corresponding isogonal deformation has an aspect ratio of 3, in good agreement with observations (Fig. 3C').

To find the tension threshold for active T1s, we calculate ℓ_{ref} using the Voronoi construction based on the vertices of the tension triangulation (see SI Sec. 1.5 for details). The length of a quartet's central interface in the Voronoi reference state is determined by the pair of tension triangles corresponding to the cell quartet (see Fig. 3D-D'). For simplicity, we consider the case of two identical, isosceles triangles which is fully characterized by the relative tension $T = 2 \sin(\phi/2)$ on the central interface, with ϕ the angle in the tension triangle. (The general case of asymmetric tensions is discussed in the companion paper [36], where we show that the T1 threshold is shifted towards stronger tension anisotropy with increasing asymmetry of the tension configurations.) In the symmetric case, the Voronoi construction for the reference length yields $\ell_{\text{ref}} = \eta T \cot(\phi)$. In the absence of isogonal deformations ($\Delta\ell_{\text{iso}} = 0$), the interface length vanishes when $\phi = \pi/2$, implying the critical relative tension $T_{\text{crit}}^0 = T_{\text{crit}}(\Delta\ell_{\text{iso}} = 0) = \sqrt{2} \approx 1.41$ (see Fig. 3D'). In general, the condition $\ell_{\text{ref}}(T) = -\Delta\ell_{\text{iso}}$ for the neighbor exchange defines the “T1 threshold” in the $\Delta\ell_{\text{iso}}-T$ plane (see Fig. 3E). This diagram quantifies how active and passive forces interact to drive cell intercalations. Active tension dynamics and passive isogonal strain appear as orthogonal ways to drive T1s, as illustrated by the red and blue arrows.

In the lateral ectoderm, in particular near the VF (purple region in Fig. 1A), DV oriented interfaces are stretched due to VF invagination. The average isogonal contribution to interface length $\langle \Delta\ell_{\text{iso}} \rangle \approx 1.9 \mu\text{m}$ of DV oriented interfaces in the lateral ectoderm can be estimated from the tissue-scale isogonal strain there (see Tissue Scale section below). One can read off the predicted relative tension threshold $T_{\text{crit}} \approx 1.53$ in Fig. 3. This is in excellent agreement with the value found by tension inference (Fig. 2D). For *twist* and *snail* mutants where the VF is abolished [55] such that there is no isogonal stretching of the lateral ectoderm, we predict a T1 threshold $T_{\text{crit}} \approx \sqrt{2}$ for active T1s. This implies that there will be no tension jump between the contracting and the extending interface for active T1s.

Minimal local model based on tension feedback reproduces length- and tension-dynamics of T1s

We conclude our analysis of intercalating cell quartets by condensing the insights gained into a parsimonious model that combines tension dynamics with a constitutive relation for the isogonal modes. Importantly, we model the dynamics in adiabatic force balance, i.e. on a timescale where the relaxation of elastic energy has already come to its conclusion. That means that the positions of the vertices do not follow an explicit dynamical equation (like the overdamped energy relaxation dynamics in a classical vertex model) but are instead implicitly determined by the tension triangulation and the isogonal modes. The dynamics resides in the changes in tension that transform and remodel the tension triangulation.

To keep the number of parameters and variables (degrees of freedom) in the model to a minimum, we consider a quartet of cells with identical shapes. This describes a representative quartet in a periodic cell array. Such a cell array is characterized by the three angles at each vertex, ϕ_i , and the three interface lengths ℓ_i , with $i \in \{0, 1, 2\}$ (see Fig. 4A). The vertex angles are determined by the relative cortical tensions T_i via the force balance condition (see Fig. 3A). Motivated by the nonlinearly increasing tension observed on contracting interfaces (cf. Fig. 2D), we equip each interface with self-reinforcing tension dynamics

$$\tau_T \partial_t T_i = T_i^n - \frac{1}{3} \sum_k T_k^n, \quad (2)$$

which models tension-induced myosin recruitment [26] (with excitability exponent n set to $n = 4$ in our simulation). The dynamics conserves the total active tension

$\sum_i T_i$, corresponding to a finite myosin pool in each cell. (Other choices for fixing the overall scale of tension, e.g. via the triangle area, as well as well as other values of n do not change the results qualitatively; see Ref. [36].) The timescale of tension dynamics τ_T is fitted to the experimental data. Positive feedback drives the relative tension on the quartet's central interface towards the tension threshold discussed above (see Fig. 4B) and thus drives active T1s. The interface that collapses is the one that starts with the highest initial tension, which we label with $i = 0$ by convention such that $T_0 > T_{1,2}$.

To find the physical cell shape for given cortical tensions, we need to determine the interface lengths ℓ_i , i.e. fix the isogonal mode (Fig. 4C). To this end, we introduce a cell elastic energy which is the isogonal mode must minimize. This elastic energy accounts for internal structures of the cell such as the nucleus and microtubuli. We assume the scale of this to be much smaller than the elastic energy due to cortical tensions. Because of this separation of scales, the angles at vertices are fixed by tensions, and the relaxation of the cell elastic energy only affects isogonal modes. We write the cell elastic energy in terms of the deviation of the cell “shape tensor” $\mathbf{S}_C = \sum_i (\mathbf{e}_i \otimes \mathbf{e}_i) / \ell_i$ from a target shape tensor \mathbf{S}_0 :

$$E_C = \lambda [\text{Tr}(S_C - S_0)]^2 + \mu \text{Tr}[(S_C - S_0)^2]. \quad (3)$$

Here, \mathbf{e}_i are the interface vectors with lengths $|\mathbf{e}_i| = \ell_i$ (see Fig. 4A) and \otimes denotes the tensor product. We choose this shape tensor because it is linear in interface length, meaning that it does not change if an interface is subdivided by inserting an additional vertex. The coefficients λ and μ control the cell's resistance to isotropic compression/dilation and shear deformations, respectively (see SI Sec. 3 for details). Notably, this elastic energy does not engender an “energy barrier” for T1 transitions as is found in vertex models with area–perimeter elasticity [56] (see also Fig. S9D). Therefore, our simulations do not require stochastic fluctuations to drive T1s.

The model described thus far captures the dynamics up to the neighbor exchange (time < 0 in Fig. 4E and F) and qualitatively reproduces the dynamics of interface length and tension observed in the experimental data (cf. Fig. 2D). Interface contraction during an active T1 is driven by active remodeling of the force balance geometry: Myosin recruitment increases the cortical tension and thus drives it out of force balance with the external tension from adjacent interfaces. As a result, the interfaces remodel, changing the angles at vertices until force balance is reestablished. Positive tension feedback continually causes further myosin recruitment, which in turn drives further contraction until the interface has fully collapsed.

How does the subsequent resolution and interface elongation work? On the emerging interface, there is typically little myosin [23, 57]. Therefore, active contractility cannot balance the external tension exerted on the interface by its neighbors: The new interface is thrown out of active force balance. This force imbalance naturally leads to the extension of the new edge. As the interface extends, passive tension bearing elements of the cytoskeleton, such as crosslinkers, get loaded until force balance is reestablished. To account for this, we split the total cortical tension T into the myosin-borne, active tension T_{myo} and the passive tension T_p . Cortical remodeling due to turnover of crosslinkers will gradually relax this passive tension. We account for this by an exponential decay $T_p \propto e^{-t/\tau_p}$ with a characteristic remodeling rate τ_p . This passive tension effectively represents Maxwell-type viscoelasticity of the extending interface, illustrated by the spring and dashpot in Fig. 4D.

Completing the model requires to understand what sets the initial motor protein level on an emerging interface, which will set the initial condition for the tension dynamics on that interface. We propose a myosin “handover” mechanism based on the assumption that the myosin level along the cortex within each cell changes continuously along the interfaces and across vertices [58] (see Fig. 4D). (Force balance requires that the total tension, the sum of the tensions in the two abutting cortices, is uniform along an interface. However, the individual tensions on either side can be non-uniform, as the resulting traction forces are exchanged via E-cadherin

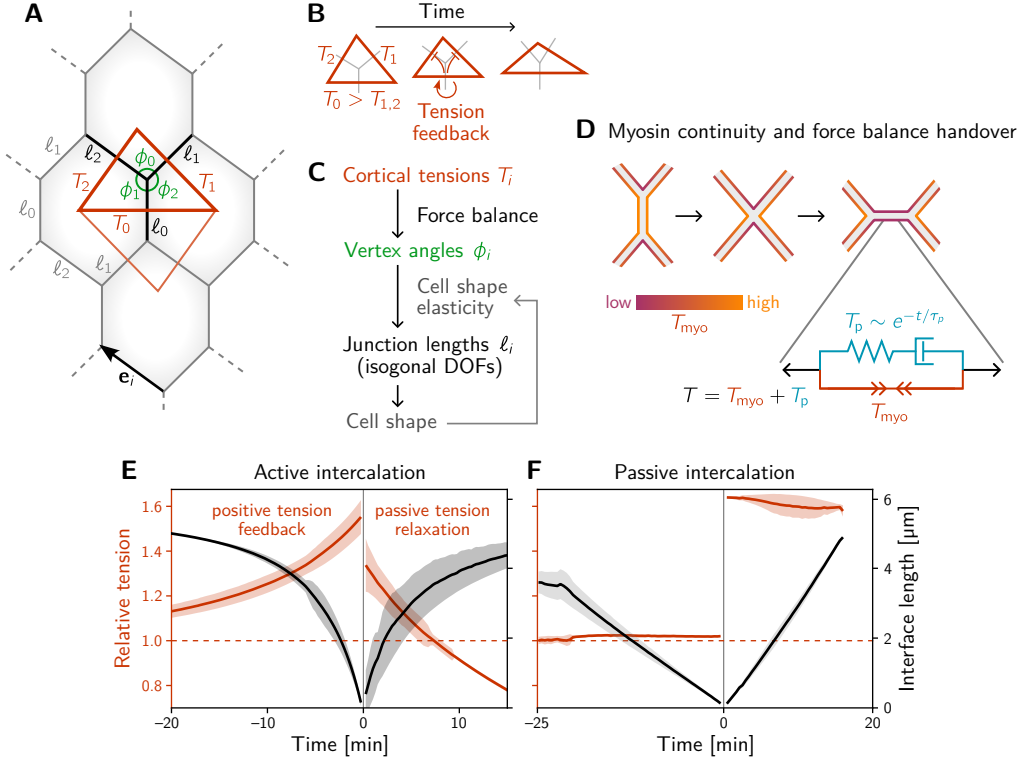


Figure 4: A minimal model for positive tension feedback reproduces the signatures of active T1s, and creates passive T1s when feedback is turned off.

A Single cell quartet of identical cells forms the elementary setting for modelling T1s. This geometry is characterized by two vertex angles (ϕ_0, ϕ_1 , and $\phi_2 = 2\pi - \phi_0 - \phi_1$) and three interface lengths (ℓ_i). The interface angles are determined by the pair of identical tension triangles corresponding to the cell quartet. To avoid boundary effects, the cell quartet and tension triangles are set up to tile the plane periodically as a regular lattice.

B Positive tension feedback causes the longest edge in a tension triangle to grow at the expense of the shorter two edges, thus deforming the triangle to become increasingly obtuse. (We fix the total tension scale. In real cells, the overall tension scale is set by the available myosin pool. Relative tensions change as myosin is redistributed between the cortex at different interfaces.)

C The tension triangle shape determines the vertex angles, ϕ_i . To fix the interface lengths ℓ_i , we determine the cell shape by minimizing an elastic energy while keeping angles fixed (see SI for details).

D Two-sided architecture of junctional cortex determines myosin level on newly formed interface. Sketch of intercalating quartet with myosin in each cell's cortex color-coded. After a neighbor exchange, the active tension (i.e. myosin level) on the new edge is determined by a “handover” mechanism that assumes continuity of myosin concentration at vertices within each cell. As consequence, the active tension on the new edge right after the neighbor exchange is below the total tension that is determined by geometry. This tension imbalance causes the new edge to extend by remodeling. To capture the remodeling, we introduce a passive viscoelastic tension T_{passive} , due to passive cortical crosslinkers. T_{passive} decays exponentially with a characteristic remodeling time τ_p . Notably, no additional active ingredients (like medial myosin contractility) are required to drive extension of the new edge.

E and F The model reproduces the signatures of active and passive T1s observed in the *Drosophila* embryo. The tension feedback rate and passive relaxation rate are fitted to match the observed timescales. (Bands show the standard deviation from an ensemble of simulations with initial angles drawn from the experimental vertex angle distribution at 0 min.)

molecules linking the cells along the interface [33].) Importantly, this “handover” model predicts that the myosin level (*not* the total tension) on the newly formed interface is always lower than that on the collapsing interface, in agreement with experimental observations [23, 57].

Simulating this model, we find good qualitative agreement between the single-quartet model and experimental data, both for the tension dynamics (compare Fig. 4E,F and Fig. 2D,E) and for the tension-isogonal decomposition (compare Fig. S9A,A' and Fig. 3C,C'). Movie 3 shows the simulation of an active T1 transition for a symmetric quartet. In the absence of positive tension feedback, the model successfully describes passive intercalations when the displacements of cell centroids are prescribed to mimic external stresses (Fig. 4F; see SI Sec. 3 for details).

Notably, in our model there is no additional active mechanism for interface extension. Instead, interface extension is a consequence of the fundamental temporal asymmetry of T1 processes: high myosin levels on the collapsing interface versus low myosin levels on the emerging interface. No additional active ingredients are required. In passing, we note that we have ignored myosin fluctuations in the above arguments. If these fluctuations are strong compared to the average myosin levels, they may cause the collapse of the emerging interface, thereby reversing a T1, as observed in some genetic mutants [47].

Tissue scale

Our analysis so far has focused on the mechanism of individual T1 transitions in cell quartets. To bridge the gap from cell quartets to tissue-scale convergent-extension flow, we need to address three key questions: (i) How are active T1s oriented? (ii) Which regions of the tissue deform actively due to internally generated local tension and which ones yield passively to stresses created by adjacent regions? (iii) How are active T1s coordinated across cells, so that different interfaces do not “attempt” to execute incompatible T1s? In the following, we will address these three questions by building on the tools (tension inference and tension-isogonal decomposition) we employed above to analyze intercalating cell quartets.

Initial anisotropy of tension directs flow

Convergent-extension flow of tissue requires that the T1 transitions are oriented. If cortical tensions are regulated by positive feedback, the tissue-scale tension anisotropy sets the orientation the interfaces which will collapse, and hence, the direction of tissue flow. Therefore, tissue-scale anisotropy of active tension is central to drive and orient convergent-extension flow [10, 57, 59, 60].

We assess tension anisotropy by locally averaging the anisotropy of inferred tensions \mathbf{T}_{ij} at a given individual vertices as illustrated in Fig. 5A (see SI for details). The inferred tension anisotropy (Fig. 5B) and its time course (Fig. 5C) are consistent with previously published experimental observations: During VF invagination, DV oriented interfaces in the lateral ectoderm are stretched causing myosin recruitment [28]. Remarkably, we find strong DV alignment of tension anisotropy in the trunk already before VF invagination (Fig. 5D, 0 min). This confirms our hypothesis that tension anisotropy is set up in the initial condition. As GBE progresses, the DV alignment of tension anisotropy decreases (Fig. 5C and Fig. 5D, 37 min). Numerical simulations presented in the companion paper [36] reproduce this loss of global tension anisotropy and show that it is responsible for the slow down of GBE after two-fold extension.

Isogonal strain identifies regions of passive tissue deformation

We started our investigation by a “tissue tectonics” analysis [24] that identifies the contributions of cell intercalations and cell shape changes to tissue deformations. This kinematic quantification in itself is not informative of the mechanical forces

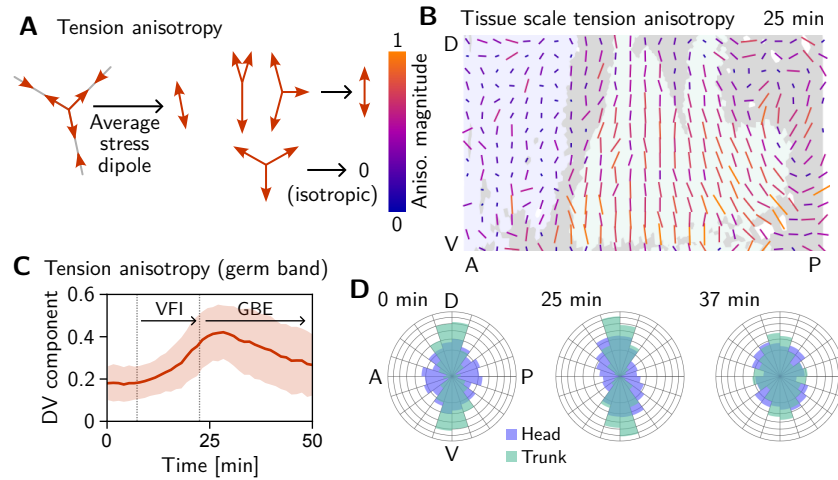


Figure 5: Tissue scale tension anisotropy orients convergent-extension flow.
A Local anisotropy of tension (double-ended arrow) at a single tri-cellular vertex.
B Tension anisotropy at the end of VF invagination/onset of GBE (25 min) locally averaged on a grid with 20 μm spacing. Line segments indicating the local orientation and magnitude (length and color of the line segments) of tension anisotropy.
C Mean DV component of locally averaged anisotropic tension in the trunk (green region in **B**). (DV component measured along a fixed axis orthogonal to the long axis of the embryo; Shading shows SD.)
D Significant DV alignment of the tension orientation in the trunk precedes any tissue flow, while the tension in the head shows no orientation bias (0 min). The DV alignment of tension slightly increases during VF invagination (25 min) and decreases during GBE (37 min).

driving epithelial dynamics. To quantify the relative contributions of active (local) vs passive (non-local) forces acting on intercalating cell quartets we introduced the tension-isogonal decomposition (Fig. 3C). Just as a tissue tectonics analysis, this decomposition can be performed on the scale of entire tissue regions without the need to track cells and identify T1 events. Specifically, we exploit the fact that the isogonal strain tensor can be calculated for each individual triplet of cells that meet at a vertex (see Fig. 6A and SI Sec. 1.5 for details). Locally averaging over nearby vertices then yields the tissue-scale isogonal deformation (see Fig. 6B and B'). At the end of VF invagination (25 min), significant isogonal strain has built up adjacent to the VF indicating that the tissue there is passively stretched by the invaginating VF (see purple shaded region in Fig. 6B). The lateral ectoderm further away from the VF also accumulates some isogonal extension along the DV axis (green shaded region, see time traces in Fig. 6E). This causes an increase of the tension threshold for active T1s (cf. Fig. 3E).

During GBE, the isogonal strain near the ventral furrow relaxes back to nearly isotropic, suggesting that the passive deformation stored in the isogonal mode is elastic rather than plastic (Fig. 6B' and C). At the same time, the actively contracting lateral ectoderm stretches the dorsal tissue (amnioserosa) along the DV axis. This passive deformation of the amnioserosa is consistent with the transition of cells from columnar to squamous [15] and low myosin density in the amnioserosa [10]. Taken together, isogonal strain identifies regions where passive tissue deformation is caused by mechanical coupling across the tissue.

A geometric order parameter quantifies local tension configurations

Tissue-scale tension anisotropy is not enough to drive coherent “parallel” T1s. Such coordination requires an alternating pattern of high and low tensions as seen in Fig. 7A (center; cf. Fig. 2C'). In contrast, when several connected interfaces are

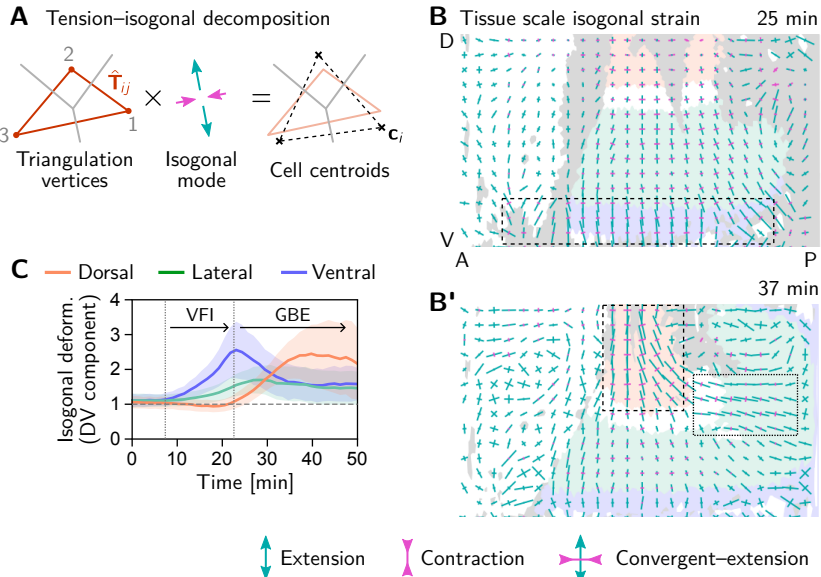


Figure 6: Tissue scale quantification of isogonal strain identifies regions of passive tissue deformation. **A** Tension–isogonal decomposition at a single tri-cellular vertex. The isogonal strain tensor (illustrated by blue arrows) transforms the tension triangle (solid red lines) into the centroidal triangle (dashed black lines). **B and B'** Isogonal strain at the end of VF invagination (25 min, B) and during GBE (37 min, B') averaged over vertices in a grid with 20 μm spacing. High isogonal strain in the tissue adjacent to the VF at 25 min and in the amnioserosa at 37 min indicate passive tissue deformations in these regions (highlighted by dashed rectangles). High isogonal strain is also found near the posterior midgut (dotted rectangle). Crosses indicate the principal axes of isogonal strain. Bar lengths indicate the magnitude of strain (green: extensile, magenta: contractile). Colored tissue regions are quantified in (C). **C** Time traces of the DV component of isogonal strain. The isogonal (i.e. passive) stretching of the tissue adjacent to the VF (purple) is transient. The lateral ectoderm as a whole (green and blue) is stretched weakly, but persistently. The amnioserosa (red) is strongly stretched as the lateral ectoderm contracts along the DV axis during GBE. (DV component is defined with respect to the local co-rotating frame, see SI; Shaded bands show one SD; SEM is comparable to the line width.)

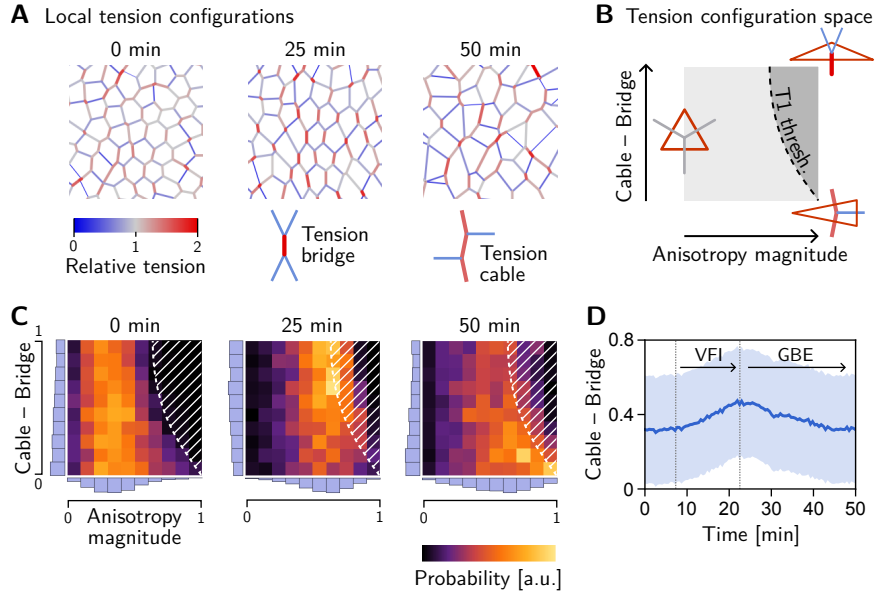


Figure 7: Emergence and loss of order in local tension configurations. **A** Distinct configurations of tension are found on the cell scale: “Tension bridges”, characterized by a high-tension interface connected to four low-tension interfaces, are the local motif of an alternating pattern of high and low tensions. This alternating pattern gives rise to coordinated T1s as the high-tension interfaces collapse, driven by positive tension feedback. By contrast, tension cables, characterized by multiple adjacent high-tension interfaces, cause frustrated or incoherent T1s which manifest as rosettes. **B** Space of local tension configurations at a single vertex (quantified by the tension triangle shape, see Ref. [36] and SI Sec. 1.7 for details). The dashed line indicates the “T1 threshold” calculated for the average isogonal strain in the germ band (cf. Fig. 3G). This threshold is at lower anisotropy magnitude for tension bridges than for tension cables, indicating that the former are more efficient at driving active intercalations. **C** Distribution of tension configurations defines an order parameter that quantifies the relative abundance of tension cables and bridges in the lateral ectoderm. Arrows highlight the increasing fraction of tension bridges before GBE (0–25 min) and its decrease during GBE (25–50 min). **D** Median of the obtuse-acute triangle shape parameter in the lateral ectoderm. (Shading shows SD; SEM is smaller than the line width.)

under high tension, they form a tension cable, contraction of which leads to rosette formation [26, 61]. Tension patterns do not appear globally with perfect regularity, but rather as local motifs that can be distinguished based on the tension configuration at individual vertices. These configurations correspond to characteristic triangle shapes in the tension triangulation (see Fig. 7B): The elementary motif of the alternating tension pattern is a “tension bridge” where a high tension interface is surrounded by low tension interfaces (see Fig. 7A, right), corresponding to an obtuse triangle (Fig. 7B, top right). In contrast, an acute tension triangle (Fig. 7F, bottom right) corresponds to the local motif of a tension cable, where neighboring interfaces along the cable are under high tension while those transverse to the cable are under low tension (see Fig. 7A, left). We can therefore use the tension triangle shape to define a *local tension configuration* (LTC) parameter. The LTC-parameter space (i.e. the space of triangle shapes), shown in Fig. 7B, is spanned by two axes, measuring how elongated and how acute or obtuse the tension triangle is (see Ref. [36], Fig. S7 and SI Sec. 1.7 for details). These axes correspond to the magnitude of local tension anisotropy and the cable vs bridge character of the local tension configuration, respectively.

LTC order choreographs T1s

The geometric condition for neighbor exchanges discussed above (cf. Fig. 3E) defines a threshold in the LTC-parameter space (dashed line in Fig. 7B, see [36] for details). When the shapes of a pair of adjacent tension triangles cross this threshold, the interface corresponding to the triangles’ shared edge collapses, giving rise to a T1 transition. From the position of the T1 threshold in the LTC-parameter space, it is immediately evident that for tension cables (acute tension triangles), the tension anisotropy required to cross the T1 threshold is higher compared to tension bridges. Tension cables are therefore less efficient at driving T1s: they require stronger anisotropy of tension to cause an interface collapse.

Two-dimensional histograms of the LTC-parameter distribution in the lateral ectoderm show that the fraction tension of bridges increases before the onset of GBE (see Fig. 7C). The bridge fraction reaches its maximum around 25 min, just at the onset of GBE (see Fig. 7D). The corresponding alternating pattern of tensions is clearly visible in Fig. 7A (center). This suggests that the pattern of tensions on the (sub-)cellular scale is biologically relevant to choreograph parallel T1s. As the tension anisotropy increases (cf. Fig. 5C), the local tension configurations eventually hit the T1 threshold where a cell neighbor exchange happens, causing a reconfiguration of local tensions. Therefore, tension configurations beyond the T1 threshold are strongly suppressed (hatched region in Fig. 7C). We observe that as cell intercalations take place in the lateral ectoderm, the fraction of tension bridges decreases and the fraction of tension cables increases (see Fig. 7G, 50 min; and Fig. 7H). In fact, the distribution of tension triangle shapes appears to approach that of a random Delaunay triangulation (see SI Fig. S8), a completely disordered distribution. This suggests that the triangle edge flips can be statistically understood as a random “mixing” process that generically causes a loss of LTC order and global alignment of tension anisotropy.

Discussion

Cortical tensions drive and constrain tissue deformations on the cellular scale

We have developed a novel perspective on tissue dynamics based on the underlying principle of force balance. Central to our approach is the balanced network of active forces generated and transmitted by cells. In epithelia where contractility in the adherens-junctional cortex is the strongest source of stress, the force network takes the form of a triangulation in tension space [12] which fixes the angles at tri-cellular

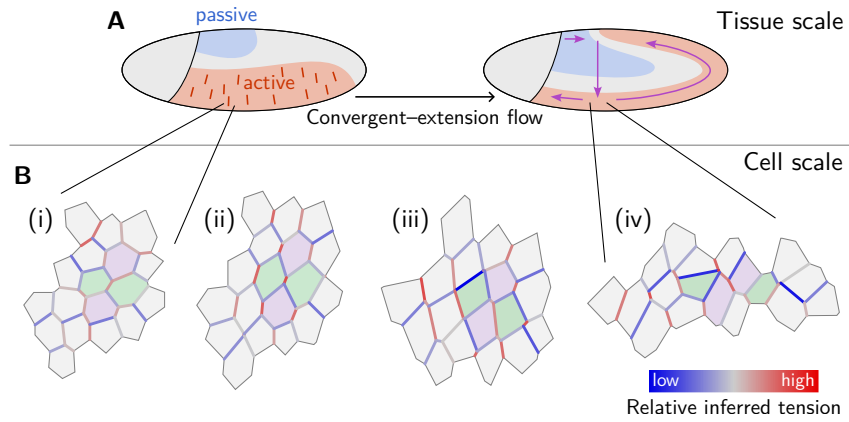


Figure 8: Mechanical coordination of convergent-extension flow on the tissue and cell scale. **A** Dorso-ventral patterning of mechanical properties and tension anisotropy (red lines) organize and orient tissue flow. **B** A cell scale pattern of tensions coordinates active cell intercalations that drive convergent extension of the lateral ectoderm. From relatively uniform but weakly anisotropic initial tensions (i), an alternating pattern of high and low tensions emerges (ii). Subsequently, high-tension interfaces fully contract thereby driving parallel active T1 transitions (iii). As T1s proceed, order in the tension configurations is lost and convergent-extension flow cedes (iv).

vertices in the tissue. Tissue deformations are driven by the adiabatic transformation of this force-balance geometry, allowing the epithelium to rearrange like a fluid, while supporting internal tension like a solid. Alternatively, one can think of this behavior as a form of plasticity where the internal “reference” structure of the material can be actively remodelled, resulting in spatial displacement of material points. Yet, the focus on the geometry of the force balance associated with the internal structure is more useful as it holds the key to understanding possible mechanisms of active control. We find two mechanically distinct modes of tissue deformation: a cortical-tension driven mode and an isogonal (angle preserving) mode that is unconstrained by the cortical force-balance geometry. The former represents active remodeling of interfaces, e.g. by myosin recruitment, while the latter accounts for passive tissue deformations that are controlled by external (non-local) forces and cell shape elasticity. The *tension-isogonal decomposition* quantifies the contributions of these two modes in experimental data based on cell geometry alone. This allows us to disentangle whether deformations are due to locally or non-locally generated forces, i.e. whether they are active or passive. Importantly, tension-isogonal decomposition is based on the same assumptions as tension inference which has been validated extensively in previous literature [34, 35, 42, 43].

In the early *Drosophila* embryo, we observe both active and passive T1s. Generally, both modes—tension-driven and isogonal—interact and contribute to tissue deformations at the same time. We have found that ventral furrow invagination isogonally stretches the lateral ectoderm which increases the tension threshold for active T1s there. We predict that the local relative tension threshold will be lower (namely $\sqrt{2}$) in mutants which lack a ventral furrow (*twist* and *snail* [55]).

Cells orchestrate tissue flow by self-organizing in tension space

How can local behavior of cells orchestrate global tissue flow? Cells exert active stresses on each other and, at the same time, constantly sense their mechanical environment [62–64]. Mechanical stresses and strains can propagate over long distances and contain information about the tissue geometry (e.g. in the form of hoop stresses [65]). In an epithelium dominated by cortical tensions, this mechanical environment is a tension space, linked to physical space via force balance. Tension space takes the form of a triangulation which allows an intuitive visualization.

The angles in the cell tessellation are fixed by complementary angles in the tension triangulation. Thus, the tensions are geometric dials cells can directly sense and control.

We found that cells can control their configuration in tension space by defining local dynamics of cortical tension. In experimental data from gastrulating *Drosophila* embryos, we identified two distinct behaviors: (i) amplification of tension on the interfaces that area already most tense, suggestive of positive tension feedback (observed in lateral ectoderm) and (ii) apparent tension homeostasis (observed in the amnioserosa). Mechanical homeostasis is found in various systems and organisms [66–68]. We hypothesize that tension homeostasis allows the amnioserosa to undergo large cell deformations while maintaining tissue integrity [67, 69]. Tension feedback, on the other hand, continuously modifies local force balance, driving the change in cell and tissue geometry. To the extent that cortical responses can be controlled by spatially modulated gene expression, evolution thus has the means to define a program of non-trivial spatio-temporal dynamics of tissue during morphogenesis. Evidence for positive feedback is provided by the nonlinearly increasing inferred tension on contracting interfaces (Fig. 2D) and by laser ablation experiments in earlier work [26]. The underlying molecular mechanisms are yet to be identified and might rely on the catch-bond behavior of myosin [70, 71] or mechano-sensitive binding of α -catenin [72, 73].

We have found that T1 events can be explained quantitatively by a simple geometric criterion which defines a “T1 threshold” in terms of the local tension configuration and the local isogonal strain. A minimal mathematical model of an intercalating cell quartet demonstrates how positive tension feedback can drive the tensions towards this T1 threshold and thus generate active T1s. In contrast, passive T1s result from external forces changing the isogonal modes until a cell neighbor exchange occurs, while tensions (and thus interface angles) remain constant.

Our mathematical model for an intercalating cell quartet also sheds light on the long-standing puzzle of how interfaces extend after a neighbor exchange, even though cortical myosin can only exert contractile forces. We show that no additional active mechanism is necessary. Our minimal model captures interface extension as a purely passive process. In our model, interface extension during both active and passive intercalations is driven by the tension on adjacent interfaces which exceeds the low active contractility of the new edge. The low myosin level on the emerging interface is predicted by a simple model for the myosin “handover” during a neighbor exchange. In tissue-scale simulations [36], the model reproduces experimental observations (interface extension even if tissue extension is blocked, generation of irregular cell shapes) that were previously taken as evidence for actively driven interface extension [29, 74].

Our findings on the dynamics of interface length and tension during active T1s (Fig. 2D) are similar to another recently proposed model [48]. This model extends the classical “vertex model” with perimeter-area elasticity by active cortical contractility. Like in our model, active T1s are driven by a positive feedback loop of cortical tension. Since our model is formulated in adiabatic force balance, it requires fewer parameters than the one of Ref. [48] and might be obtained in the limit of fast mechanical relaxation from the latter.

Order in local tension configurations coordinates active T1s

We found a striking alternating pattern of cortical tensions that explains how T1s are coordinated between neighboring cells. The prevalence of this organizing motif is quantified by an order parameter for local tension configurations (LTC). LTC order precedes intercalations in lateral ectoderm and the loss of LTC order correlates with the slowdown of tissue flow at the end of GBE. This raises two important questions: First, how does LTC order emerge? Second, is loss of LTC order the cause for the termination GBE? These questions are addressed in a companion paper [36] using a tissue-scale mathematical model based on the quartet-scale model

introduced here. We show that LTC order is driven by positive tension feedback and requires an initial regular hexagonal packing of cells. Intercalations disrupt this regular hexagonal packing and thus lead to the loss of LTC order as GBE progresses. Together with a degradation of coherent tension orientation, loss of LTC order causes T1s to become incoherent and therefore ineffective at driving tissue flow. Taken together, this implies that convergent-extension flow is self-limiting and that the final tissue shape is encoded in the initial degree hexagonal order and tension anisotropy. Moreover, we predict that disrupting the hexagonal packing of nuclei prior to cellularization will prevent the emergence of LTC order and thus cause slower GBE.

Genetic patterning and initial anisotropy

Because *Drosophila* embryo is a closed surface, convergent extension of the germ band must be compensated by an orthogonal deformation of the dorsal tissue, the amnioserosa (see Fig. 6B'). To achieve that, mechanical properties of the tissue must be modulated along the dorso-ventral axis: Positive tension feedback driving active rearrangements in the lateral ectoderm, and tension homeostasis in the amnioserosa allowing it to yield to external forces while maintaining tissue integrity. This highlights the importance of the DV-axis patterning. Recent work [28] has shown that mechanical feedback loops in the embryo are patterned along the DV axis. Notably, the DV patterning system is conserved across species [75]. Our work also highlights a second interaction between tissue flow and DV patterning: because the coherent T1s we observe do not scramble cells in the tissue (Fig. 1A), distinct DV fates (e.g. neural and surface ectoderm) do not mix, a clear biological necessity.

In addition to the DV gradient, tension anisotropy along the DV axis is required to orient the GBE flow along the AP axis. This anisotropy might be due to mechanics (pulling of the ventral furrow [28] and hoop stresses resulting from ellipsoidal embryo geometry [65], since we observe anisotropy already prior to VF formation), or indeed due to AP-striped genetic patterning [76, 77]. Thanks to the positive tension feedback, a weak initial anisotropy is sufficient to bias the direction of tissue elongation. This explains why *twist* and *snail* mutants, which have significantly reduced initial myosin anisotropy, still extend their germ band, albeit at a slower rate [28].

Our findings show how genetic patterning and self-organization are interconnected during GBE. Genetic patterning provides tissue scale input by demarcating distinct tissue regions with different mechanical properties. Self-organization via positive tension feedback orchestrates myosin contractility on the cellular scale and drives T1s. In the companion paper [36], we show that mechanical self-organization via tension feedback also allows cells to coordinate their behaviors (such as active T1s) with their neighbors. As of yet, no genetic mechanism has been found that produces cell scale coordination—as manifested, for instance, in the alternating pattern of high and low tensions (Fig. 7A, center)—from predetermined genetic patterns alone. Instead, the emerging overarching picture is that of morphogenesis driven by an interplay of bottom-up self-organization and top-down genetic patterning [5, 78].

Going forward, we expect that geometric insight into tension space will provide a new perspective on many different systems [79], for example *Xenopus* neural tube formation [80], amniote primitive streak formation [9, 81, 82], wing disk elongation [83, 84], the sea urchin archenteron [85], or kidney tubule elongation [86]. Further, it will be interesting to study intercalations driven by actin “protrusions” [87]: they too are governed by cortical force balance on the cellular level, making tension inference and the tension-isogonal decomposition applicable.

Acknowledgements. We thank Matthew Lefebvre, Noah Mitchell, Sebastian Streichen, and Arthur Hernandez for stimulating discussions and careful reading of the manuscript. FB acknowledges support of the GBMF post-doctoral fellowship

(GBMF award #2919). NHC was supported by NIGMS R35-GM138203 and NSF PHY:1707973. EFW acknowledges support from Howard Hughes Medical Institute. BIS acknowledges support via NSF PHY:1707973 and NSF PHY:2210612.

References

- [1] Mao, Y. *et al.* Planar polarization of the atypical myosin Dachs orients cell divisions in *Drosophila*. *Genes & Development* **25**, 131–136 (2011). URL <http://genesdev.cshlp.org/lookup/doi/10.1101/gad.610511>.
- [2] Gillies, T. E. & Cabernard, C. Cell Division Orientation in Animals. *Current Biology* **21**, R599–R609 (2011). URL <https://linkinghub.elsevier.com/retrieve/pii/S0960982211007287>.
- [3] Huebner, R. J. & Wallingford, J. B. Coming to Consensus: A Unifying Model Emerges for Convergent Extension. *Developmental Cell* **46**, 389–396 (2018). URL <https://linkinghub.elsevier.com/retrieve/pii/S1534580718306397>.
- [4] Oster, G. F., Murray, J. D. & Harris, A. K. Mechanical aspects of mesenchymal morphogenesis. *Development* **78**, 83–125 (1983). URL <https://journals.biologists.com/dev/article/78/1/83/51263/Mechanical-aspects-of-mesenchymal-morphogenesis>.
- [5] Schweisguth, F. & Corson, F. Self-Organization in Pattern Formation. *Developmental Cell* **49**, 659–677 (2019). URL <https://linkinghub.elsevier.com/retrieve/pii/S1534580719303910>.
- [6] Palmquist, K. H. *et al.* Reciprocal cell-ECM dynamics generate supracellular fluidity underlying spontaneous follicle patterning. *Cell* **185**, 1960–1973.e11 (2022). URL <https://linkinghub.elsevier.com/retrieve/pii/S0092867422004706>.
- [7] Caldarelli, P., Chamolly, A., Alegria-Prévot, O., Gros, J. & Corson, F. Self-organized tissue mechanics underlie embryonic regulation. *bioRxiv* doi:10.1101/2021.10.08.463661 (2021). URL <http://biorxiv.org/lookup/doi/10.1101/2021.10.08.463661>.
- [8] Ferenc, J. *et al.* Mechanical oscillations orchestrate axial patterning through Wnt activation in *Hydra*. *Science Advances* **7**, eabj6897 (2021). URL <https://www.science.org/doi/10.1126/sciadv.abj6897>.
- [9] Saadaoui, M., Rocancourt, D., Roussel, J., Corson, F. & Gros, J. A tensile ring drives tissue flows to shape the gastrulating amniote embryo. *Science* **367**, 453–458 (2020). URL <https://www.science.org/doi/10.1126/science.aaw1965>.
- [10] Streichan, S. J., Lefebvre, M. F., Noll, N., Wieschaus, E. F. & Shraiman, B. I. Global morphogenetic flow is accurately predicted by the spatial distribution of myosin motors. *eLife* **7**, e27454 (2018). URL <https://elifesciences.org/articles/27454>.
- [11] Ma, X., Lynch, H. E., Scully, P. C. & Hutson, M. S. Probing embryonic tissue mechanics with laser hole drilling. *Physical Biology* **6**, 036004 (2009). URL <https://iopscience.iop.org/article/10.1088/1478-3975/6/3/036004>.
- [12] Noll, N., Mani, M., Heemskerk, I., Streichan, S. J. & Shraiman, B. I. Active tension network model suggests an exotic mechanical state realized in epithelial tissues. *Nature Physics* **13**, 1221–1226 (2017). URL <https://www.nature.com/articles/nphys4219>.

- [13] Hales, K. G., Korey, C. A., Larracuente, A. M. & Roberts, D. M. Genetics on the Fly: A Primer on the *Drosophila* Model System. *Genetics* **201**, 815–842 (2015). URL <https://academic.oup.com/genetics/article/201/3/815/5930114>.
- [14] Krzic, U., Gunther, S., Saunders, T. E., Streichan, S. J. & Hufnagel, L. Multiview light-sheet microscope for rapid *in toto* imaging. *Nature Methods* **9**, 730–733 (2012). URL <http://www.nature.com/articles/nmeth.2064>.
- [15] Stern, T., Shvartsman, S. Y. & Wieschaus, E. F. Deconstructing gastrulation at single-cell resolution. *Current Biology* **32**, 1861–1868.e7 (2022). URL <https://linkinghub.elsevier.com/retrieve/pii/S0960982222003293>.
- [16] Heemskerk, I. & Streichan, S. J. Tissue cartography: Compressing bio-image data by dimensional reduction. *Nature Methods* **12**, 1139–1142 (2015). URL <http://www.nature.com/articles/nmeth.3648>.
- [17] Gilbert, S. F. & Barresi, M. J. F. *Developmental Biology* (Sinauer Associates, Sunderland, Massachusetts, 2016).
- [18] Leptin, M. Drosophila Gastrulation: From Pattern Formation to Morphogenesis. *Annual Review of Cell and Developmental Biology* **11**, 189–212 (1995). URL <https://www.annualreviews.org/doi/10.1146/annurev.cb.11.110195.001201>.
- [19] Martin, A. C., Kaschube, M. & Wieschaus, E. F. Pulsed contractions of an actin–myosin network drive apical constriction. *Nature* **457**, 495–499 (2009). URL <http://dx.doi.org/10.1038/nature07522>.
- [20] Martin, A. C. The Physical Mechanisms of Drosophila Gastrulation: Mesoderm and Endoderm Invagination. *Genetics* **214**, 543–560 (2020). URL <http://www.genetics.org/lookup/doi/10.1534/genetics.119.301292>.
- [21] Irvine, K. & Wieschaus, E. Cell intercalation during Drosophila germband extension and its regulation by pair-rule segmentation genes. *Development* **120**, 827–841 (1994). URL <https://journals.biologists.com/dev/article/120/4/827/38309/Cell-intercalation-during-Drosophila-germband>.
- [22] Zallen, J. A. & Wieschaus, E. F. Patterned Gene Expression Directs Bipolar Planar Polarity in Drosophila. *Developmental Cell* **6**, 343–355 (2004).
- [23] Bertet, C., Sulak, L. & Lecuit, T. Myosin-dependent junction remodelling controls planar cell intercalation and axis elongation. *Nature* **429**, 667–671 (2004). URL <http://www.nature.com/articles/nature02581>.
- [24] Blanchard, G. B. *et al.* Tissue tectonics: Morphogenetic strain rates, cell shape change and intercalation. *Nature Methods* **6**, 458–464 (2009). URL <http://www.nature.com/articles/nmeth.1327>.
- [25] Lecuit, T., Lenne, P.-F. & Munro, E. Force Generation, Transmission, and Integration during Cell and Tissue Morphogenesis. *Annual Review of Cell and Developmental Biology* **27**, 157–184 (2011). URL <https://www.annualreviews.org/doi/10.1146/annurev-cellbio-100109-104027>.
- [26] Blankenship, J. T., Backovic, S. T., Sanny, J. S., Weitz, O. & Zallen, J. A. Multicellular Rosette Formation Links Planar Cell Polarity to Tissue Morphogenesis. *Developmental Cell* **11**, 459–470 (2006). URL <https://linkinghub.elsevier.com/retrieve/pii/S153458070600400X>.
- [27] Fernandez-Gonzalez, R., Simoes, S. d. M., Röper, J.-C., Eaton, S. & Zallen, J. A. Myosin II Dynamics Are Regulated by Tension in Intercalating Cells. *Developmental Cell* **17**, 736–743 (2009). URL <http://www.nature.com/articles/s41556-020-0524-x>.

- [28] Gustafson, H. J., Claussen, N., De Renzis, S. & Streichan, S. J. Patterned mechanical feedback establishes a global myosin gradient. *bioRxiv* doi:10.1101/2021.12.06.471321 (2021). URL <http://biorxiv.org/lookup/doi/10.1101/2021.12.06.471321>.
- [29] Collinet, C., Rauzi, M., Lenne, P.-F. & Lecuit, T. Local and tissue-scale forces drive oriented junction growth during tissue extension. *Nature Cell Biology* **17**, 1247–1258 (2015). URL <http://www.nature.com/articles/ncb3226>.
- [30] Rauzi, M. Cell intercalation in a simple epithelium. *Philosophical Transactions of the Royal Society B: Biological Sciences* **375**, 20190552 (2020). URL <https://royalsocietypublishing.org/doi/10.1098/rstb.2019.0552>.
- [31] Gehrels, E. W., Chakrabortty, B., Perrin, M.-E., Merkel, M. & Lecuit, T. Curvature gradient drives polarized tissue flow in the *Drosophila* embryo. *Proceedings of the National Academy of Sciences* **120**, e2214205120 (2023). URL <https://pnas.org/doi/10.1073/pnas.2214205120>.
- [32] Vanderleest, T. E. *et al.* Vertex sliding drives intercalation by radial coupling of adhesion and actomyosin networks during Drosophila germband extension. *eLife* **7**, e34586 (2018). URL <https://elifesciences.org/articles/34586>.
- [33] Chiou, K. K., Hufnagel, L. & Shraiman, B. I. Mechanical Stress Inference for Two Dimensional Cell Arrays. *PLoS Computational Biology* **8**, e1002512 (2012). URL <https://dx.plos.org/10.1371/journal.pcbi.1002512>.
- [34] Ishihara, S. *et al.* Comparative study of non-invasive force and stress inference methods in tissue. *The European Physical Journal E* **36**, 45 (2013). URL <http://link.springer.com/10.1140/epje/i2013-13045-8>.
- [35] Noll, N., Streichan, S. J. & Shraiman, B. I. Variational Method for Image-Based Inference of Internal Stress in Epithelial Tissues. *Physical Review X* **10**, 011072 (2020). URL <https://link.aps.org/doi/10.1103/PhysRevX.10.011072>.
- [36] Claussen, N. H., Brauns, F. & Shraiman, B. I. A Geometric Tension Dynamics Model of Epithelial Convergent Extension. *arXiv* 2311.16384 (2023). URL <https://arxiv.org/abs/2311.16384>. **2311.16384**.
- [37] Bambadekar, K., Clément, R., Blanc, O., Chardès, C. & Lenne, P.-F. Direct laser manipulation reveals the mechanics of cell contacts in vivo. *Proceedings of the National Academy of Sciences* **112**, 1416–1421 (2015). URL <https://pnas.org/doi/full/10.1073/pnas.1418732112>.
- [38] Munjal, A., Philippe, J.-M., Munro, E. & Lecuit, T. A self-organized biomechanical network drives shape changes during tissue morphogenesis. *Nature* **524**, 351–355 (2015). URL <https://elifesciences.org/articles/10757>.
- [39] Lecuit, T. & Yap, A. S. E-cadherin junctions as active mechanical integrators in tissue dynamics. *Nature Publishing Group* **17**, 533–539 (2015). URL <http://dx.doi.org/10.1038/ncb3136>.
- [40] Prost, J., Jülicher, F. & Joanny, J.-F. Active gel physics. *Nature Physics* **11**, 111–117 (2015). URL <http://www.nature.com/articles/nphys3224>.
- [41] Doubrovinski, K., Swan, M., Polyakov, O. & Wieschaus, E. F. Measurement of cortical elasticity in *Drosophila melanogaster* embryos using ferrofluids. *Proceedings of the National Academy of Sciences* **114**, 1051–1056 (2017). URL <https://pnas.org/doi/full/10.1073/pnas.1616659114>.
- [42] Cheikh, M. I. *et al.* A comprehensive model of Drosophila epithelium reveals the role of embryo geometry and cell topology in mechanical responses. *bioRxiv* doi:10.1101/2022.08.12.503803 (2022). URL <http://biorxiv.org/lookup/doi/10.1101/2022.08.12.503803>.

- [43] Kong, W. *et al.* Experimental validation of force inference in epithelia from cell to tissue scale. *Scientific Reports* **9**, 14647 (2019). URL <https://www.nature.com/articles/s41598-019-50690-3>.
- [44] Maxwell, J. C. On reciprocal figures and diagrams of forces. *The London, Edinburgh, and Dublin Philosophical Magazine and Journal of Science* **27**, 250–261 (1864). URL <https://www.tandfonline.com/doi/full/10.1080/14786446408643663>.
- [45] Varignon, P. *Nouvelle Mécanique Ou Statique, Dont Le Projet Fut Donné En 1687: Ouvrage Posthume* (chez Claude Jombert, 1725). URL <https://books.google.com/books?id=o-1WAAAAcAAJ>.
- [46] Tighe, B. P., van Eerd, A. R. T. & Vlugt, T. J. H. Entropy Maximization in the Force Network Ensemble for Granular Solids. *Physical Review Letters* **100**, 238001 (2008). URL <https://link.aps.org/doi/10.1103/PhysRevLett.100.238001>.
- [47] Stern, T., Shvartsman, S. Y. & Wieschaus, E. F. Template-based mapping of dynamic motifs in tissue morphogenesis. *PLOS Computational Biology* **16**, e1008049 (2020). URL <https://dx.plos.org/10.1371/journal.pcbi.1008049>.
- [48] Sknepnek, R., Djafer-Cherif, I., Chuai, M., Weijer, C. & Henkes, S. Generating active T1 transitions through mechanochemical feedback. *eLife* **12**, e79862 (2023). URL <https://elifesciences.org/articles/79862>.
- [49] Ramms, L. *et al.* Keratins as the main component for the mechanical integrity of keratinocytes. *Proceedings of the National Academy of Sciences* **110**, 18513–18518 (2013). URL <https://pnas.org/doi/full/10.1073/pnas.1313491110>.
- [50] Charrier, E. E. *et al.* The desmin network is a determinant of the cytoplasmic stiffness of myoblasts: Desmin network: A determinant of the cytoplasmic stiffness of myoblasts. *Biology of the Cell* **110**, 77–90 (2018). URL <https://onlinelibrary.wiley.com/doi/10.1111/boc.201700040>.
- [51] Pensalfini, M., Golde, T., Trepat, X. & Arroyo, M. Nonaffine Mechanics of Entangled Networks Inspired by Intermediate Filaments. *Physical Review Letters* **131**, 058101 (2023). URL <https://link.aps.org/doi/10.1103/PhysRevLett.131.058101>.
- [52] Merkel, M. *et al.* Triangles bridge the scales: Quantifying cellular contributions to tissue deformation. *Physical Review E* **95**, 032401 (2017). URL <https://link.aps.org/doi/10.1103/PhysRevE.95.032401>.
- [53] Bocanegra-Moreno, L., Singh, A., Hannezo, E., Zagorski, M. & Kicheva, A. Cell cycle dynamics control fluidity of the developing mouse neuroepithelium. *Nature Physics* (2023). URL <https://www.nature.com/articles/s41567-023-01977-w>.
- [54] Priess, J. R. & Hirsh, D. I. *Caenorhabditis elegans* morphogenesis: The role of the cytoskeleton in elongation of the embryo. *Developmental Biology* **117**, 156–173 (1986). URL <https://linkinghub.elsevier.com/retrieve/pii/0012160686903581>.
- [55] Cost, M., Sweeton, D. & Wieschaus, E. Gastrulation in *Drosophila*: Cellular mechanisms of morphogenetic movements. In Martinez Arias, B. (ed.) *The Development of Drosophila Melanogaster*, 425–465 (Cold Spring Harbor Laboratory Press, 1993).

- [56] Bi, D., Lopez, J. H., Schwarz, J. M. & Manning, M. L. A density-independent rigidity transition in biological tissues. *Nature Physics* **11**, 1074–1079 (2015). URL <http://www.nature.com/articles/nphys3471>.
- [57] Rauzi, M., Verant, P., Lecuit, T. & Lenne, P.-F. Nature and anisotropy of cortical forces orienting Drosophila tissue morphogenesis. *Nature Cell Biology* **10**, 1401–1410 (2008). URL <http://www.nature.com/articles/ncb1798>.
- [58] Kale, G. R. *et al.* Distinct contributions of tensile and shear stress on E-cadherin levels during morphogenesis. *Nature Communications* **9**, 5021 (2018). URL <https://www.nature.com/articles/s41467-018-07448-8>.
- [59] Etournay, R. *et al.* Interplay of cell dynamics and epithelial tension during morphogenesis of the Drosophila pupal wing. *eLife* **4**, e07090 (2015). URL <https://elifesciences.org/articles/07090>.
- [60] Lau, K. *et al.* Anisotropic stress orients remodelling of mammalian limb bud ectoderm. *Nature Cell Biology* **17**, 569–579 (2015). URL <https://www.nature.com/articles/ncb3156>.
- [61] Harding, M. J., McGraw, H. F. & Nechiporuk, A. The roles and regulation of multicellular rosette structures during morphogenesis. *Development* **141**, 2549–2558 (2014). URL <https://journals.biologists.com/dev/article/141/13/2549/46279/The-roles-and-regulation-of-multicellular-rosette>.
- [62] Heisenberg, C.-P. & Bellaïche, Y. Forces in Tissue Morphogenesis and Patterning. *Cell* **153**, 948–962 (2013). URL <https://linkinghub.elsevier.com/retrieve/pii/S0092867413005734>.
- [63] Collinet, C. & Lecuit, T. Programmed and self-organized flow of information during morphogenesis. *Nature Reviews Molecular Cell Biology* **22**, 245–265 (2021). URL <http://www.nature.com/articles/s41580-020-00318-6>.
- [64] Pinheiro, D. & Bellaïche, Y. Mechanical Force-Driven Adherens Junction Remodeling and Epithelial Dynamics. *Developmental Cell* **47**, 3–19 (2018). URL <https://linkinghub.elsevier.com/retrieve/pii/S1534580718307433>.
- [65] Lefebvre, M. F., Claussen, N. H., Mitchell, N. P., Gustafson, H. J. & Streichan, S. J. Geometric control of myosin II orientation during axis elongation. *eLife* **12**, e78787 (2023). URL <https://elifesciences.org/articles/78787>.
- [66] Humphrey, J. D. Vascular Adaptation and Mechanical Homeostasis at Tissue, Cellular, and Sub-cellular Levels. *Cell Biochemistry and Biophysics* **50**, 53–78 (2008). URL <http://link.springer.com/10.1007/s12013-007-9002-3>.
- [67] Latorre, E. *et al.* Active superelasticity in three-dimensional epithelia of controlled shape. *Nature* **563**, 203–208 (2018). URL <http://www.nature.com/articles/s41586-018-0671-4>.
- [68] Stamenović, D. & Smith, M. L. Tensional homeostasis at different length scales. *Soft Matter* **16**, 6946–6963 (2020). URL <http://xlink.rsc.org/?DOI=D0SM00763C>.
- [69] Jodoin, J. N. *et al.* Stable Force Balance between Epithelial Cells Arises from F-Actin Turnover. *Developmental Cell* **35**, 685–697 (2015). URL <https://linkinghub.elsevier.com/retrieve/pii/S1534580715007534>.
- [70] Veigel, C., Molloy, J. E., Schmitz, S. & Kendrick-Jones, J. Load-dependent kinetics of force production by smooth muscle myosin measured with optical tweezers. *Nature Cell Biology* **5**, 980–986 (2003). URL <http://www.nature.com/articles/ncb1060>.

- [71] Laakso, J. M., Lewis, J. H., Shuman, H. & Ostap, E. M. Myosin I Can Act As a Molecular Force Sensor. *Science* **321**, 133–136 (2008). URL <https://www.science.org/doi/10.1126/science.1159419>.
- [72] Barry, A. K. *et al.* α -Catenin cytomechanics – role in cadherin-dependent adhesion and mechanotransduction. *Journal of Cell Science* **127**, 1779–1791 (2014). URL <https://journals.biologists.com/jcs/article/127/8/1779/54962/Catenin-cytomechanics-role-in-cadherin-dependent>.
- [73] Mei, L. *et al.* Molecular mechanism for direct actin force-sensing by α -catenin. *eLife* **9**, e62514 (2020). URL <https://elifesciences.org/articles/62514>.
- [74] Vanderleest, T. E., Xie, Y., Smits, C., Blankenship, J. T. & Loerke, D. Interface extension is a continuum property suggesting a linkage between AP contractile and DV lengthening processes. *Molecular Biology of the Cell* **33**, ar142 (2022). URL <https://www.molbiolcell.org/doi/10.1091/mbc.E21-07-0352>.
- [75] Holley, S. A. & Ferguson, E. L. Fish are like flies are like frogs: Conservation of dorsal-ventral patterning mechanisms. *BioEssays* **19**, 281–284 (1997). URL <https://onlinelibrary.wiley.com/doi/10.1002/bies.950190404>.
- [76] Butler, M. T. & Wallingford, J. B. Planar cell polarity in development and disease. *Nature Reviews Molecular Cell Biology* **18**, 375–388 (2017). URL <http://www.nature.com/articles/nrm.2017.11>.
- [77] Lavalou, J. *et al.* Formation of polarized contractile interfaces by self-organized Toll-8/CirI GPCR asymmetry. *Developmental Cell* **56**, 1574–1588.e7 (2021). URL <https://linkinghub.elsevier.com/retrieve/pii/S1534580721002707>.
- [78] Lenne, P.-F. *et al.* Roadmap for the multiscale coupling of biochemical and mechanical signals during development. *Physical Biology* **18**, 041501 (2021). URL <https://iopscience.iop.org/article/10.1088/1478-3975/abd0db>.
- [79] Shindo, A. Models of convergent extension during morphogenesis. *WIREs Developmental Biology* **7** (2018). URL <https://onlinelibrary.wiley.com/doi/10.1002/wdev.293>.
- [80] Butler, M. T. & Wallingford, J. B. Spatial and temporal analysis of PCP protein dynamics during neural tube closure. *eLife* **7**, e36456 (2018). URL <https://elifesciences.org/articles/36456>.
- [81] Voiculescu, O., Bertocchini, F., Wolpert, L., Keller, R. E. & Stern, C. D. The amniote primitive streak is defined by epithelial cell intercalation before gastrulation. *Nature* **449**, 1049–1052 (2007). URL <https://www.nature.com/articles/nature06211>.
- [82] Rozbicki, E. *et al.* Myosin-II-mediated cell shape changes and cell intercalation contribute to primitive streak formation. *Nature Cell Biology* **17**, 397–408 (2015). URL <http://www.nature.com/articles/ncb3138>.
- [83] Dye, N. A. *et al.* Cell dynamics underlying oriented growth of the *Drosophila* wing imaginal disc. *Development* dev.155069 (2017). URL <https://journals.biologists.com/dev/article/doi/10.1242/dev.155069/264392/Cell-dynamics-underlying-oriented-growth-of-the>.
- [84] Dye, N. A. *et al.* Self-organized patterning of cell morphology via mechanosen-sitive feedback. *eLife* **10**, e57964 (2021). URL <https://elifesciences.org/articles/57964>.

- [85] Hardin, J. & Weliky, M. Cell rearrangement induced by filopodial tension accounts for the late phase of convergent extension in the sea urchin archenteron. *Molecular Biology of the Cell* **30**, 1911–1919 (2019). URL <https://www.molbiolcell.org/doi/10.1091/mbc.E19-03-0143>.
- [86] Lienkamp, S. S. *et al.* Vertebrate kidney tubules elongate using a planar cell polarity-dependent, rosette-based mechanism of convergent extension. *Nature Genetics* **44**, 1382–1387 (2012). URL <http://www.nature.com/articles/ng.2452>.
- [87] Weng, S., Huebner, R. J. & Wallingford, J. B. Convergent extension requires adhesion-dependent biomechanical integration of cell crawling and junction contraction. *Cell Reports* **39**, 110666 (2022). URL <https://linkinghub.elsevier.com/retrieve/pii/S2211124722004181>.
- [88] Guirao, B. *et al.* Unified quantitative characterization of epithelial tissue development. *eLife* **4**, e08519 (2015). URL <https://elifesciences.org/articles/08519>.
- [89] Efrati, E., Sharon, E. & Kupferman, R. Elastic theory of unconstrained non-Euclidean plates. *Journal of the Mechanics and Physics of Solids* **57**, 762–775 (2009). URL <https://linkinghub.elsevier.com/retrieve/pii/S0022509608002160>.
- [90] Ginibre, J. Statistical Ensembles of Complex, Quaternion, and Real Matrices. *Journal of Mathematical Physics* **6**, 440–449 (1965). URL <http://aip.scitation.org/doi/10.1063/1.1704292>.
- [91] Claussen, N. CE_simulation_public, https://github.com/nikolas-claussen/CE_simulation_public (2023). URL https://github.com/nikolas-claussen/CE_simulation_public.
- [92] Virtanen et al., P. SciPy 1.0: Fundamental algorithms for scientific computing in Python. *Nature Methods* **17**, 261–272 (2020). URL <http://www.nature.com/articles/s41592-019-0686-2>.

SUPPLEMENTARY MATERIAL

1 Analysis of experimental data

1.1 Data source

Whole embryo cell segmentation and tracking data was obtained from the repository [DOI:10.6084/m9.figshare.18551420.v3](https://doi.org/10.6084/m9.figshare.18551420.v3) deposited with Ref. [15]. We analyzed the dataset with id number 1620 since it had the highest time resolution (15 s) and covered the longest time period (50 min), starting ca. 7 min before the onset of ventral furrow invagination.

1.2 Tissue tectonics analysis

Based on segmented and tracked cells, the tissue strain rate and cell deformation rate can be calculated via the methods described in Ref. [24]; see also [88] and [52]. In brief, the local tissue strain rate is calculated from the centroid positions \mathbf{c}_i of the cells in a small neighborhood N of a cell (we use nearest neighbors). One looks for a linear transformation that maps the positions of the cell centroids at one timepoint to those at the next one. Because the resulting equations are overdetermined, an approximate solution minimizing the error is obtained using the least-squares algorithm. The linear transformation is then further decomposed into a symmetric part, describing local shear and area changes, and an antisymmetric part, describing the tissue rotation. Because the *Drosophila* ectoderm is a surface in three dimensional space, we need to calculate these quantities in the local tangent plane. The cell deformation rate is calculated from the rate of change of the cell's moment of inertia tensor in the frame that co-rotates with the tissue.

Figure S1A–B' show the tissue and cell deformation rates during VF invagination (A and A') and during GBE (B and B'). Figure S1C shows the cell elongation as measured by the Beltrami coefficient $\mu = |a - b|/(a + b)$, where a and b are the half-axes of a best-fit ellipse to the cell.

Local tangent plane and coordinate frames. The analysis of local tissue geometry (including tissue tectonics, tension inference, and tension-isogonal decomposition) is performed in the local tangent plane. The local tangent plane is determined by the local normal vector \mathbf{n} which we find by a singular value decomposition of the point set of interest (vertex coordinates for a single cell, cell centroids for a patch of cells). The normal vector is read-off as the basis vector corresponding to the smallest singular value.

Depending on the context, we use three different coordinate bases within the tangent plane: (i) The “Eulerian” (or “lab frame”) basis formed by the azimuthal vector $\mathbf{e}_{\text{DV}}^{\text{E}}$ along the DV axis and its orthogonal complement $\mathbf{e}_{\text{AP}}^{\text{E}} = \mathbf{n} \times \mathbf{e}_{\text{DV}}^{\text{E}}$, along the AP axis. The Eulerian frame is used to plot orientation and strain fields in the flat map projections (“pullbacks”) of the tissue (e.g. Fig. 3D and Fig. 7B). (ii) A “Lagrangian” (or “tissue frame”) basis which co-rotates with the tissue is used to quantify the DV component of the isogonal deformation tensor (Fig. 3E). This co-rotating frame is defined by tracking a patch of cells and fitting a linear transformation $A(t)$ to the displacement of cell centroids relative to the patch’s center of mass. The linear transformation is constrained to transform the initial into the final normal vector $A.\mathbf{n}(0) = \mathbf{n}(t)$. A polar decomposition $A(t) = S(t).R(t)$ then yields the local rotation matrix $R(t)$ for the tissue patch. The co-rotated basis vectors are obtained by applying R to the Eulerian basis vectors at time zero: $\mathbf{e}_i^{\text{L}}(t) = R(t).\mathbf{e}_i^{\text{E}}(0)$. (iii) For the tension-isogonal decomposition of intercalating cell quartets (Fig. 3C and C' and Fig. S6), we define a co-moving orthogonal basis based on the cell centroids: The basis vectors are defined as the pair of orthogonal vectors that best fit the displacement vectors that connect opposite cells in the quartet. Before the neighbor exchange, the first basis vector is aligned with the

two cells that touch and the second basis vector is aligned with the cells that don't touch. After the neighbor exchange, the roles are flipped. This ensures that the basis vectors vary smoothly through the neighbor exchange.

1.3 Identification and classification of intercalation events

Cell interface collapse and emergence events can be identified by tracking cell contacts. We start by identifying all pairs of cells that share a interface at some timepoint. For each pair, one can then identify the time periods where the cells are in contact. This allows one to identify interface collapse and emergence events. We exclude cases where a cell pair loses contact because one of the cells invaginates or divides and cases where cells come into contact because cells in between them invaginate.

Some cell pairs transiently lose or gain contact. For the interface collapse rate shown in Fig. 1E, we only account for the first collapse event for cell pairs that are not in contact at the last frame, i.e. for those that *permanently* lose contact. Similarly, for interface emergence events, we only account for the last event where a pair of cells not in contact at the first frame comes into contact.

Spatial distribution of interface collapses. From the tracked interface collapses, we can count the number of interface collapses that each cell is involved in, giving us a spatially resolved map of intercalations (Fig. S1D). In the lateral ectoderm (regions 4–8 in Fig. S3A), we find 2.58 interface collapses per cell. From this, we can estimate the total tissue extension by cell rearrangements. In a hexagonal lattice, synchronous T1s cause two interface collapses per cell and elongate the tissue by a factor $\sqrt{3}$, assuming that the cells do not elongate. (The tissue also contracts by a factor $1/\sqrt{3}$ along the orthogonal axis.) For 2.58 interface collapses per cell, therefore cause tissue elongation by a factor $(2.58/2) \times \sqrt{3} \approx 2.23$, in good agreement with the total elongation of the germ band (cf. Fig. 1D).

In contrast to the lateral ectoderm where cells don't elongate coherently, cell elongation contributes significantly to tissue deformation near the dorsal pole (see Fig. S1C). This is a generic feature of passive T1s driven by isogonal deformations (see Fig. S6D).

Orientation of collapsing interfaces. The convergent-extension flows in the lateral ectoderm and near the dorsal pole (amniocerosa) are oriented perpendicular to each other (see Fig. S1). We therefore also expect perpendicular orientation of the collapsing interfaces in these two regions. We quantify interface orientation of collapsing edges at the blastoderm stage (i.e. before the onset of tissue flow, $t = 0$ min) as shown in Fig. S2A and C. In the ectoderm, interfaces that collapse before $t = 42$ min, i.e. within the first ca. 15 min of GBE are predominantly DV oriented at $t = 0$ min (see Fig. S2B). By contrast, interfaces near the dorsal pole predominantly oriented along AP. The orientation of interfaces in the lateral ectoderm that collapse after $t = 42$ min is initially not strongly biased along the DV axis (Fig. S2C and D). However, during GBE, these interfaces progressively align with the DV co-rotated DV axis before they eventually start contracting (see Fig. S2C' and D; the coordinate frame co-rotating with the tissue is described in Sec. 1.2).

Tracking quartets and identifying rosettes. The above procedure for identifying intercalation events is very fast and easy to implement. However, it does not distinguish between T1s and higher order intercalation events (rosettes). Moreover, it cannot easily be determined which interface collapse corresponds to which interface emergence.

We therefore implemented an alternative algorithm to identify intercalations, by tracking quartets of cells. This is possible by identifying cycles of length four in the neighborhood graph of the cell tessellation at each time point. We exclude cases where the four cells surround one or more cells that are not part of the cycle and

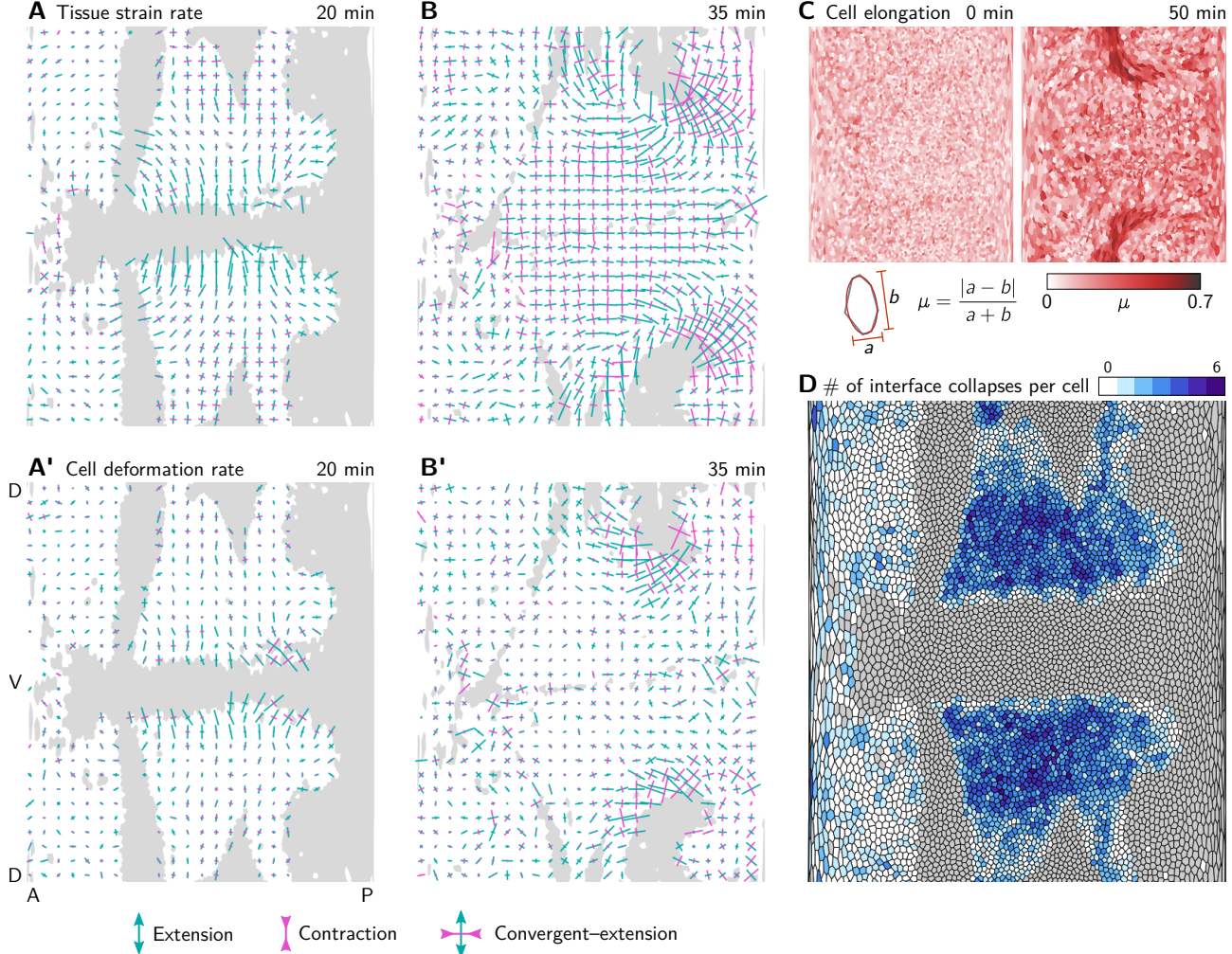


Figure S1: Tissue tectonics analysis. **A and A'** During VF invagination, the tissue strain rate (A) and cell deformation rate (A') are high in the lateral ectoderm adjacent to the ventral furrow, where cells get stretched along the DV axis. Crosses show the principal axis of strain averaged in a grid with 20 μm spacing. Bar length is proportional to the strain rate and color indicates extension (green) and convergence (magenta). **B and B'** During GBE, the tissue strain rate (B) is high in the lateral ectoderm which undergoes convergent extension. The cell deformation rate (B') there is low, and incoherent implying that the tissue deforms via cell rearrangements. In contrast, near the dorsal pole, both cell deformation and cell rearrangements contribute to tissue strain rate. **C** Cell elongation measured by the Beltrami coefficient μ from the best-fit ellipse. Cells near the dorsal pole become highly elongated. **D** Total number of interface collapses per cell. Note that in Ref. [15] (the source of the segmentation data), the number of intercalations per cell is instead calculated as the sum of collapsed interfaces and new interfaces per cell, leading to numbers higher by a factor of 2. (Invaginating cells are shown in gray. Strain rates are only shown for cells that do not invaginate.)

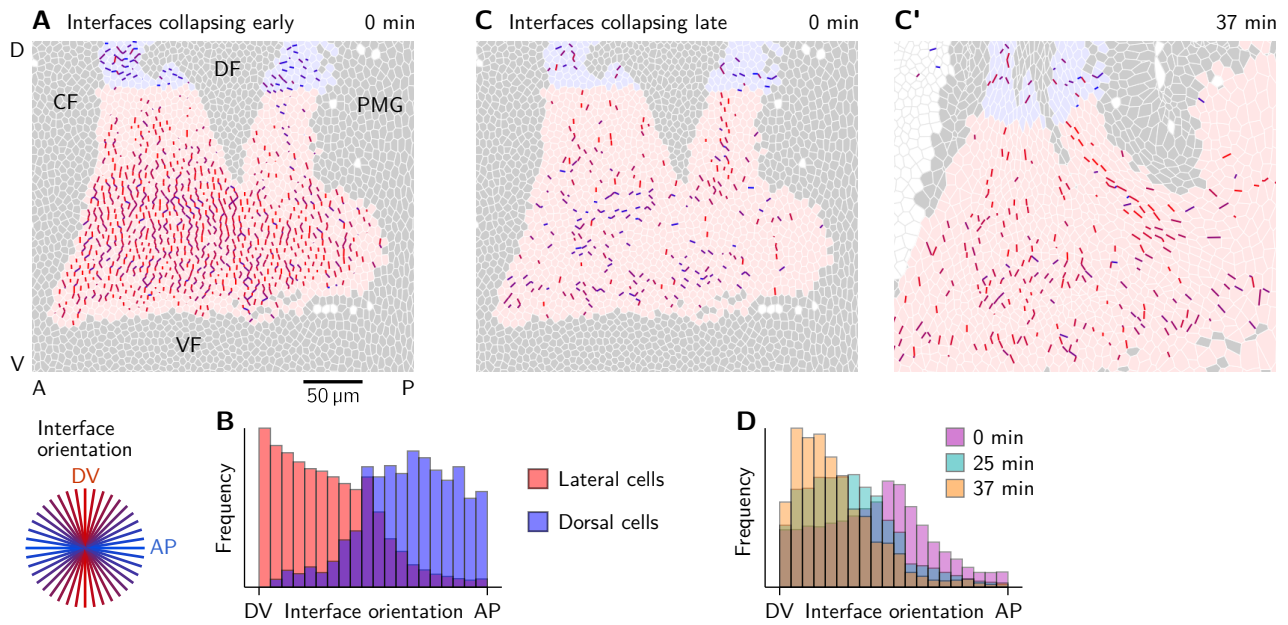


Figure S2: Orientation of collapsing interfaces. **A** and **B** interfaces collapsing early (before 42 min) colored by their orientation at time 0 min (A) and histograms showing the interface orientation (B). Collapsing interfaces near the dorsal pole (shaded blue) are predominantly oriented along the AP axis. In the lateral ectoderm, the orientation is predominantly along the DV axis. **C–D** Interfaces collapsing late (after 42 min) have low initial orientational bias (C) but progressively align with the co-rotated DV axis before they start contracting (C').

cases where one of the cells is surrounded by the three others. Notably, the quartets don't necessarily exist for the entire time series. Namely, when one of the "inner" interfaces in the quartet, other than the central interface, collapses, the quartet is destroyed.

A T1 event happens when the opposite pairs of cells in the quartet exchange neighbors (i.e. one pair loses contact and the other one gains it). In some cases, the neighbor exchange is not instantaneous, but instead there is a fourfold vertex in the center of the quartet for an extended period. Cases where the central interface and one of its neighbors are simultaneously shorter than a threshold length ($0.5 \mu\text{m}$) are classified as rosettes and not counted as T1s. The threshold value $0.5 \mu\text{m}$ corresponds to the average vertex-positions fluctuations on the timescale of 1 min. Higher order rosettes can be "decomposed" into overlapping 5-fold rosettes and therefore can be identified by finding such overlaps.

Using this procedure, we identified 2231 T1 events, 498 five-fold rosettes, 40 six-fold rosettes, 4 seven-fold rosettes and no higher order rosettes (see Fig. 1E'). Because the number of rosettes is small compared to the number of T1s, we have focused on T1 events for the subsequent analysis.

1.4 Local tension inference

Consider the triplet of cells that meet at a tri-cellular vertex and label them $i = 1, 2, 3$. Denote the unit vectors pointing along the three interfaces that meet at the vertex by \mathbf{e}_{ij} , where i, j are the labels of the pair of cells that share the respective interface. Force balance implies that

$$T_{12}\mathbf{e}_{12} + T_{23}\mathbf{e}_{23} + T_{31}\mathbf{e}_{31} = 0, \quad (4)$$

where T_{ij} are the cortical tensions. Multiplying the above equation with $\hat{\mathbf{e}}_{12}$ and $\hat{\mathbf{e}}_{23}$ (where $\hat{\mathbf{e}}$ denotes the vector orthogonal to \mathbf{e} and with the same magnitude)

yields two equations

$$\begin{aligned} T_{23} \sin \alpha_{123} - T_{31} \sin \alpha_{312} &= 0, \\ T_{12} \sin \alpha_{123} - T_{31} \sin \alpha_{231} &= 0. \end{aligned} \quad (5)$$

Here, α_{ijk} denotes the angle subtended by the interfaces (ij) and (jk) . These equations do not constrain the overall level of tension. We fix this by setting the average tension to 1 which gives the solution. These equations are solved by

$$T_{12} = \mathcal{N} \sin \alpha_{231}, \quad T_{23} = \mathcal{N} \sin \alpha_{312}, \quad T_{31} = \mathcal{N} \sin \alpha_{123}, \quad (6)$$

with the normalization factor $a = \sum_{(ijk)} \sin \alpha_{ijk}$.

The above calculation can be generalized to an arbitrary number of vertices. Notably, the equations become overconstrained once the set of vertices contains entire cells [12]. This is because force balance implies that the tension vectors $\mathbf{T}_{ij} = T_{ij} \mathbf{e}_{ij}$ form a triangulation (see below).

Here, we limit ourselves to local tension inference for the central interface in a cell quartet (see Fig. 2A). In this case, the equations are not overconstrained. Labelling the cells 1–4, the equations read

$$\begin{aligned} T_{23} \sin \alpha_{123} - T_{13} \sin \alpha_{312} &= 0, \\ T_{12} \sin \alpha_{123} - T_{13} \sin \alpha_{231} &= 0, \\ T_{34} \sin \alpha_{143} - T_{13} \sin \alpha_{314} &= 0, \\ T_{14} \sin \alpha_{143} - T_{13} \sin \alpha_{431} &= 0. \end{aligned} \quad (7)$$

We solve these equations with the additional constraint that the average of the T_{12}, T_{23}, T_{34} and T_{14} is 1. The solution for “inner” cortical tension T_{13} then is that relative to the average tension of its neighbors. We call this the *relative tension* of a interface in the following.

Analysis of collapsing and emerging interfaces. For the analysis presented in Fig. 2D and E, collapsing and emerging interfaces were identified separately as described in Sec. 1.3. All events before 12 min were excluded from the analysis.

When a interface is short, the interface angles become highly susceptible to fluctuations of the vertex positions. We therefore excluded all timepoints where the central interface or one of its neighbors is shorter than a threshold length (0.75 μm). This value was chosen because the vertex positions fluctuate about 0.5 μm between timepoints. These fluctuations are partially due to intrinsic fluctuations in cortical tension and partially result from limitations in vertex localization during segmentation because of limited optical resolution.

Time series of interface length and relative tension are then aligned such that the interface collapse (respectively emergence) is at $t = 0$. Figure S3 shows the pooled data resolved by the position of the quartet along the DV axis.

1.5 Tension-isogonal decomposition

Because the angles in the tension triangulation are complementary to the interfacial angles in the cell tessellation, one can find a unique tension triangulation (up to a global scale factor) for a given physical cell tessellation in force balance (see dashed gray arrow in Fig. S6A). However, the reverse is not true. For a given tension triangulation, there is a continuous family of cell tessellations that share the same tension triangulation and that are related by *isogonal* deformations which change the interface lengths collectively while preserving the angles. (Mathematically, there are fewer triangulation vertices than cell vertices, so that the triangulation leaves one isogonal mode degree of freedom per cell undetermined. We will use this in Sec. 2 to define an “isogonal potential” that parametrizes the isogonal modes.)

The isogonal degrees of freedom reflect tissue deformations that are not constrained by force balance of cortical tensions. This means that weaker contributions

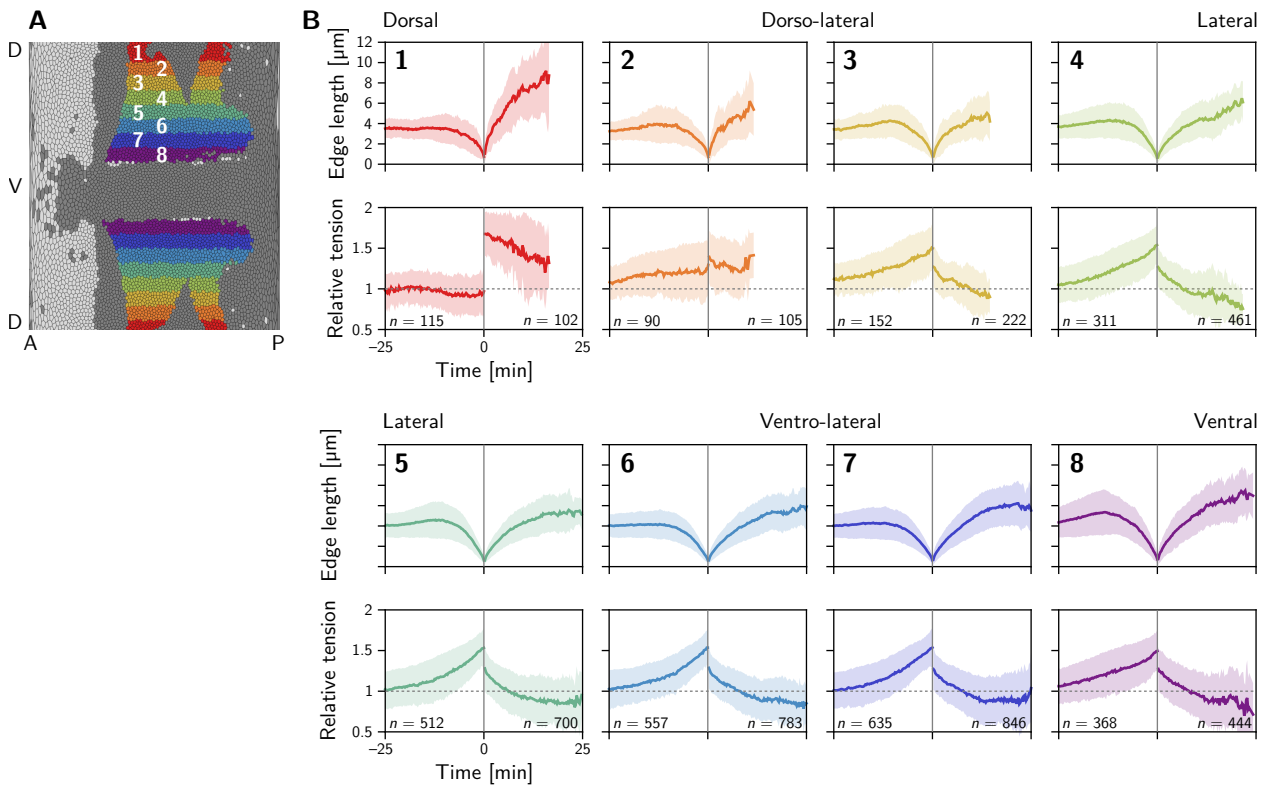


Figure S3: Length and relative tension of the central interface in intercalating cell quartets resolved by DV position. Two distinct classes of behavior are found: in the dorsal-most region (1), the relative tension remains constant at one on the contracting interface and jumps to a high value ($\approx \sqrt{3}$) on the collapsing interface where it slowly relaxes back towards one. In contrast in the lateral ectoderm (regions 3–8), relative tension increases nonlinearly during interface contraction while the tension on the emerging interface starts at a lower value and rapidly relaxes to a value below one. Region 2 is an exception and appears to fall between the two above cases. Collapsing and emerging interfaces were analyzed separately, such that the numbers of events do not match exactly between them. Events are counted as part of a stripe when at least one of the two cells that come into contact comes from that stripe. Because cells converge along the DV axis in the lateral ectoderm, this implies that many interface emergence events are double counted there which inflates the number of emergence events relative to the collapse events.

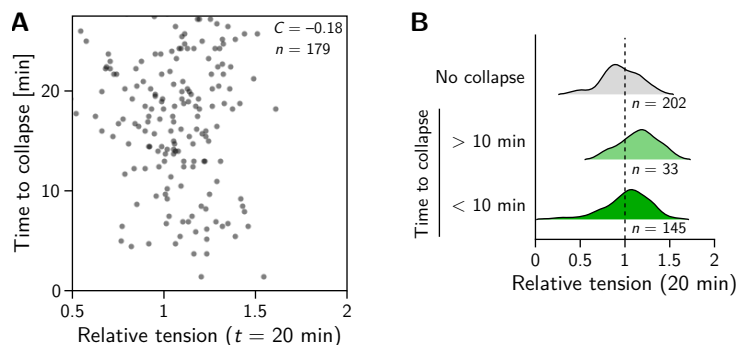


Figure S4: **A** In the amnioserosa relative tension is not correlated with the time until a interface collapses. **B** The distribution of relative tensions on interfaces that collapse is similar to those that persist. Compare to Fig. 2H and J for the quantification of interface collapses in the lateral ectoderm.

to stress, e.g. from intermediate filaments, microtubules and the nucleus in the cell interior, as well as externally applied stresses will drive the isogonal modes. This has two important consequences: (i) For the analysis of experimental data, it implies that we can decompose the tissue deformations into active, tension-driven and passive, isogonal contributions. (ii) For modeling, it implies that we need to specify a cell shape elasticity to fix the isogonal modes (see Sec. ?? and Sec. 3 below).

In the following, we discuss the details of the *tension-isogonal decomposition*. To achieve a well-defined decomposition of tissue deformation, we need to specify a reference tessellation that is uniquely determined by the tension triangulation. There will then be a unique isogonal deformation that deforms the reference configuration into the physical cell tessellation. Fortunately, we do not need to explicitly construct the reference configuration. Rather, we use the triangulation formed by the cell centroids to quantify the physical tissue shape [52]. (This implies to some degree of coarse-graining, as information about the non-affine displacements of individual vertices is lost.) We can then obtain the isogonal deformation by comparing the tension triangulation to the centroidal triangulation.

Single-vertex level. To make this construction concrete, we first consider a single tri-cellular vertex, with the associated tension triangle $\hat{\mathbf{T}}_{ij}$ and the centroids \mathbf{c}_i . The indices $i, j = 1, 2, 3$ label the three cells that meet at the vertex (see Fig. S5A'). The tension triangle vectors $\hat{\mathbf{T}}_{ij}$ are obtained by local tension inference based on the interface unit vectors \mathbf{e}_{ij} (see Sec. 1.4) and a subsequent rotation of the tension vectors by $\pi/2$. To fix the tension scale, we normalize the area of the tension triangle to one. Fixing the tension triangle area is justified because it maintains the total area of the tension triangulation such that cell dilation/contraction are purely isogonal.¹

We define the local isogonal deformation tensor $\mathbf{I}_{\text{vertex}}$ such that it transforms the tension triangle into the centroidal triangle. Mathematically, this definition is written as the equations $\eta \mathbf{I}_{\text{vertex}} \cdot \hat{\mathbf{T}}_{ij} = \mathbf{c}_j - \mathbf{c}_i, i \neq j \in \{1, 2, 3\}$. The scale factor η converts units of tension (a.u.) into units of length. How we fix η is described below.

Because the isogonal modes must preserve angles, they cannot include rotations. In other words, $\mathbf{I}_{\text{vertex}}$ must be a symmetric tensor, and therefore has only 3 degrees of freedom. However, the above equations impose 4 constraints. We therefore determine $\mathbf{I}_{\text{vertex}}$ using least squares, i.e. by solving the minimization problem

$$\min_{\mathbf{I}_{\text{vertex}} \in \text{Sym}_2} \sum_{(ij)} \|\eta \mathbf{I}_{\text{vertex}} \cdot \hat{\mathbf{T}}_{ij} - \mathbf{d}_{ij}\|^2 \quad (8)$$

where Sym_2 is the set of symmetric 2×2 matrices.

Fixing the scale factor η . To fix η we use that the tension triangles are initially close to equilateral (as evidenced by the angle distribution peaked around $\pi/3$, see Fig. 7L). For an equilateral triangle, the edge length is determined by the area, which we have normalized to one, giving an edge length $2/3^{1/4} \approx 1.52$. The average edge length of the centroidal triangles is given by the average centroid distance between adjacent cells, which we find to be $6.38 \mu\text{m}$. The ratio of these two numbers gives a scale factor $\eta \approx 4.2 \mu\text{m}$. This scale factor minimizes the isogonal strain at $t = 0$ (see Fig. S5B). Indeed, minimizing $\langle \|\mathbf{I}\| \rangle$ at a reference time provides a more general way to determine η in cases where the initial triangulation is not as uniform and regular as in the *Drosophila* blastoderm.

Coarse-grained isogonal strain. To find the tissue scale isogonal strain, we coarse grain the isogonal deformation tensor on a square grid in the flat map projection (“pullback”). The grid spacing is set to $20 \mu\text{m}$, such that each grid facet

¹The numerical value of the tension triangle area is immaterial, since it can be absorbed in the scale factor η .

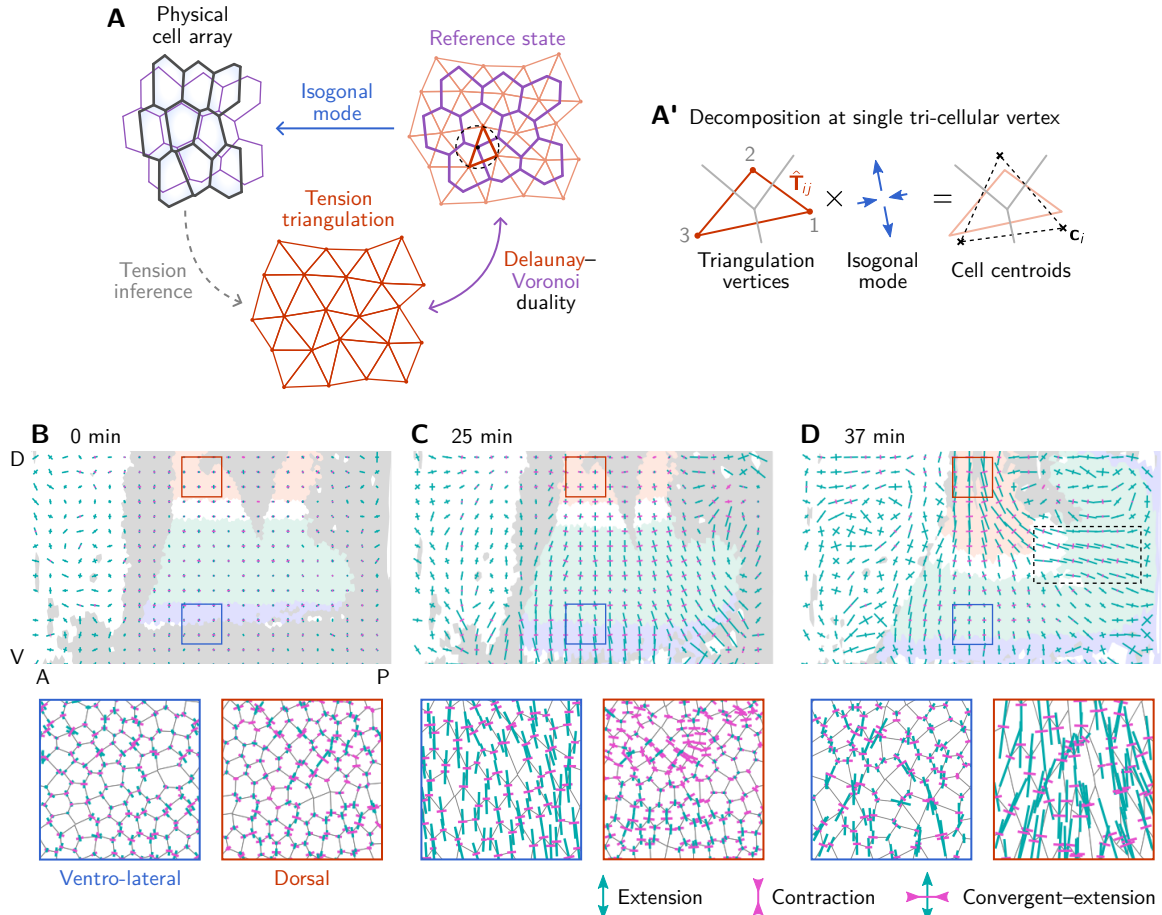


Figure S5: Tension-isogonal decomposition: Single-vertex analysis and coarse graining. **A** To a given tension triangulation (red), a corresponding dual cell tessellation is obtained via the Voronoi construction (purple), which is based on the circumcircles of the triangles. Because the tension triangulation fixes only the angles, it leaves freedom for *isogonal* (angle-preserving) modes that collectively change the interface lengths. Deformations of the tissue can be decomposed into deformations of the tension triangulation and isogonal deformations. **A'** The tension-isogonal decomposition at a single vertex based on the tension triangulation vectors $\hat{\mathbf{T}}_{ij}$ and the cell centroids \mathbf{c}_i . The indices i, j label the three cells that meet at the vertex. **B–D** Coarse-grained isogonal strain (top) and isogonal strain at individual vertices (insets) for different timepoints. The initial isogonal strain (B) is minimized to fix the scale factor η . During VF invagination, the lateral ectoderm close to the ventral furrow is stretched (C). During GBE, the isogonal strain in the lateral ectoderm remains approximately constant while the amnioserosa gets stretched. Crosses show the principal axes of the local isogonal strain tensor. Bar length indicates the amount of strain (green = extension, magenta = contraction). Coarse-grained strain tensors were averaged on a grid with spacing 20 μm . Insets show regions with size 50 \times 50 μm^2 .

contains ca 10–15 cells (grid facets near the poles contain less cells because of the distortion caused by the pullback projection). We calculate $\mathbf{I}_{\text{vertex}}$ for all tri-cellular vertices in a grid facet and take the average to find $\mathbf{I}_{\text{facet}}$.

Figures 3D and S5B–D (top panels) show the isogonal strain tensor $\mathbf{I}_{\text{facet}} - \mathbb{I}$, where \mathbb{I} is the identity matrix. The bottom panels in Fig. S5B–D show the individual, single-vertex strain tensors $\mathbf{I}_{\text{facet}} - \mathbb{I}$ at each vertex. Crosses indicate the principal eigenvectors of the strain tensors. The bar length is proportional to the eigenvalue. Green (magenta) indicates a positive (negative) eigenvalue, i.e. contraction (elongation).

To calculate the average isogonal deformation in different tissue regions (Fig. 3E), we first transform the single-vertex isogonal deformation tensor to the local co-rotating (“Lagrangian”) frame (see Sec. 1.2). This is important because the germ band rotates as it moves over the posterior pole during elongation.

To estimate the critical tension for T1s in the lateral ectoderm, we need the average isogonal contribution to the length of DV-oriented interfaces, $\langle \Delta\ell_{\text{iso}} \rangle$ (see SI Sec. 1.5). At the end of VF invagination ($t = 25$ min), we find $\langle (\mathbf{I}_{\text{vertex}})_{22} \rangle \approx 1.538 \pm 0.006$, where the index 2 denotes the DV component and the average is taken over cells in the lateral ectoderm (region shaded in blue in Fig. S5C). We thus have $\langle \Delta\ell_{\text{iso}} \rangle = (\mathbf{I}_{22} - 1)\langle \ell(0) \rangle \approx 1.9 \mu\text{m}$ for DV-oriented interfaces, where $\langle \ell(0) \rangle \approx 3.5 \mu\text{m}$ is the average initial interface length.

Filtering of degenerate tension triangles. When one of the angles at a vertex is close to π , the tension triangle becomes highly elongated. In fact, sometimes one of the angles at a vertex exceeds π due to fluctuations and inaccuracies in detection. In the tension inference, this leads to negative tensions. The (nearly) degenerate tension triangles, in turn lead to extreme apparent local isogonal deformations. We therefore exclude nearly degenerate tension triangles whose perimeter is larger than 8 after normalizing the area to 1 (ca. 2% of the tension triangles are filtered out this way).

Quartet shape tensors. The tension–isogonal decomposition for cell quartets is calculated analogously to the procedure for single vertices. The two tension triangles associated to the inner vertices of the cell quartet form a “kite” (see Fig. S6A). We normalize tension such that the average area of the tension triangles is one. The quartet’s isogonal deformation tensor $\mathbf{I}_{\text{quartet}}$ is defined such that it transforms the vectors \mathbf{T}_{ij} into the corresponding centroidal displacement vectors $\mathbf{c}_j - \mathbf{c}_i$. Here, we only use the vectors around the perimeter of the tension and centroidal kite. This ensures that the isogonal deformation tensor varies continuously through the cell neighbor exchange where the inner edge in the kite is flipped. As in the single-vertex case, we find $\mathbf{I}_{\text{quartet}}$ using least squares.

To quantify the deformations of the tension kite and the physical cell quartet, we define the shape tensors

$$\mathbb{G}_{\text{T}} = \eta^2 \sum_{(ij)} \hat{\mathbf{T}}_{ij} \otimes \hat{\mathbf{T}}_{ij}, \quad (9)$$

$$\mathbb{G}_{\text{C}} = \sum_{(ij)} (\mathbf{c}_i - \mathbf{c}_j) \otimes (\mathbf{c}_i - \mathbf{c}_j), \quad (10)$$

where the index pairs (ij) run over cell pairs going around the quartet, i.e. $(ij) = (12), (23), (34), (41)$. Notably, with these definitions, one has the relation

$$\mathbf{I}_{\text{quartet}} \cdot \mathbb{G}_{\text{T}} \cdot \mathbf{I}_{\text{quartet}} \approx \mathbb{G}_{\text{C}}. \quad (11)$$

Remarks on the Voronoi construction for the reference cell tessellation. For the tension–isogonal decomposition, we have circumvented the explicit construction of a reference cell tessellation by directly comparing the tension triangulation

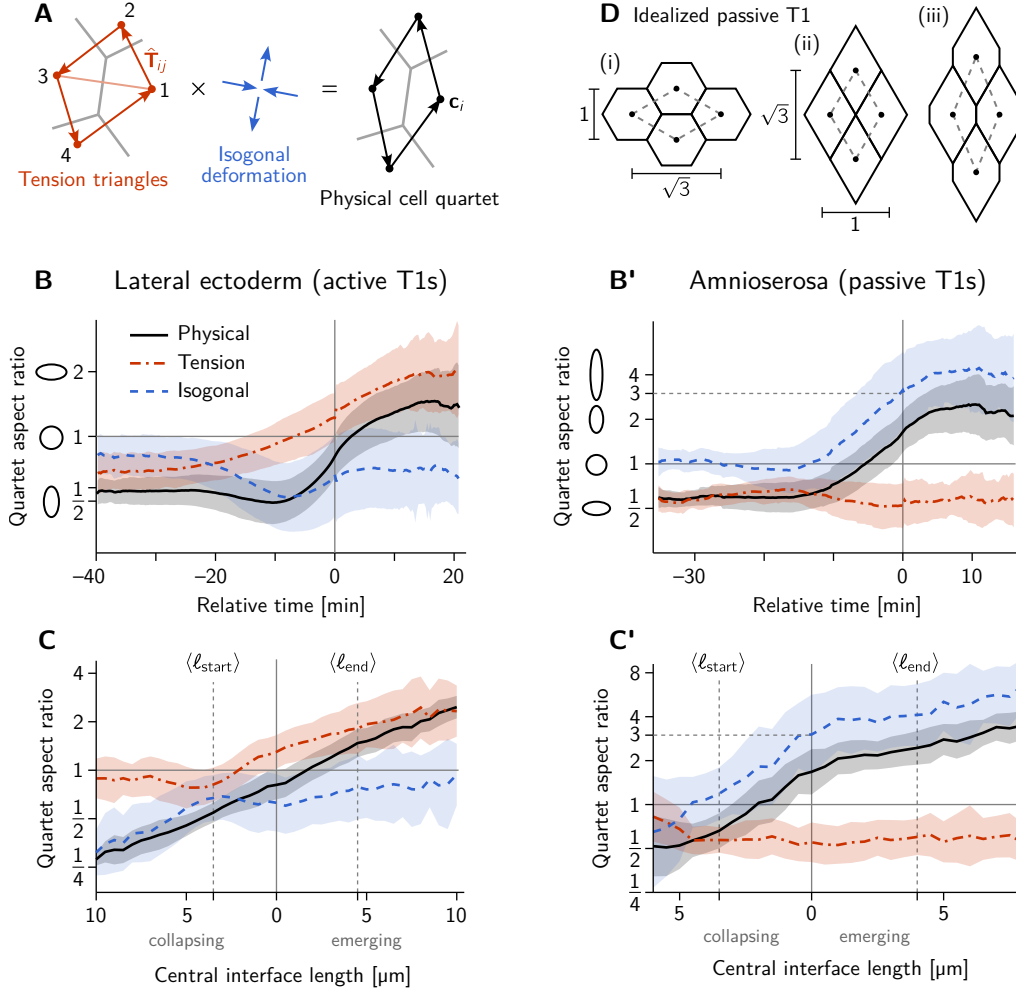


Figure S6: **A** Tension–isogonal decomposition for a cell quartet. The isogonal deformation is defined as the tensor that deforms the “kite” formed by the tension vectors \mathbf{T}_{ij} into the corresponding centroidal kite, formed from the cell centroids \mathbf{c}_i . The indices (ij) label the four cell pairs going around the kite: (12), (23), (34), (41). **B–C'** Quartet aspect ratio and eigenvalue ratio of the isogonal deformation tensor as a function of time relative to the T1 event (B and B') and as a function of the central interface’s length (C and C'). The isogonal deformation seen in B from -20 to -10 min and in C for collapsing edge lengths $> 4 \mu\text{m}$ is driven by the VF invagination which stretches the germ band.) **D** Passive intercalation of an idealized cell quartet composed of regular hexagons: (i) initial configuration; (ii) four-fold vertex configuration after area-preserving isogonal shear changing the aspect ratio by a factor 3; (iii) further isogonal deformation after the neighbor exchange. Black disks mark the cell centroids used to define the quartet shape (see A).

to the centroidal triangulation of the physical cells. This approach is particularly useful because a local isogonal deformation tensor can be obtained on the level of a single tri-cellular vertex.

The explicit construction of the reference cell tessellation allows us understand the geometry of cell-neighbor exchanges and find a criterion for when they occur (see main text for a discussion simple symmetric case and the companion paper [36] for the general case). We define the reference tessellation using a generalized Voronoi construction based on the tension triangulation. The vertices of this generalized Voronoi tessellation are given by the circumcircle centers of the triangles in the triangulation. The generalized Voronoi tessellation is only free of self-intersections when the triangulation fulfills the Delaunay criterion that opposite angles in adjacent triangles must sum to a value smaller than π . As we will see, in the following section, this provides a purely geometric criterion for neighbor exchanges in the absence of isogonal strain. In the presence of isogonal strain, the reference can have self intersections (i.e. negative interface lengths). This is similar to how the reference state encoding plastic deformations in finite strain theory isn't necessarily geometrically compatible [89].

In general, the centroids of the generalized Voronoi cells will not coincide with the vertices of the tension triangulation. This means that the definition of the isogonal deformation tensor based on the tension triangulation vertices is not exactly identical to that based on an explicit Voronoi construction. However, the two agree for a periodic lattice of identical tension triangles. In this case, the vertices of the tension triangulation coincide exactly with the centroids of the generalized Voronoi tessellation. In other words, using the tension triangulation vertices to define isogonal deformations amounts to approximating tissue as locally lattice-like, which is valid when spatial gradients are small on the cell scale.

In passing, we note that the generalized Voronoi tessellation is not the only possible reference state. Any tessellation that is uniquely defined by a given tension triangulation is in principle a valid reference state. The Voronoi tessellation is a useful choice for the following analysis because the Voronoi cell shapes behave similar to the actual cell shapes and because it is defined purely geometrically. Other choices of the reference state might be of use depending on the particular question and when one has more detailed information about the mechanical properties of the cells.

1.6 Local tension anisotropy

From the tension vectors \mathbf{T}_{ij} at a vertex, we calculate the “tension anisotropy” tensor

$$\mathbb{T} = \frac{1}{\mathcal{N}^2} \sum_{(ij)} \mathbf{T}_{ij} \otimes \mathbf{T}_{ij} \quad (12)$$

where the sum runs over pairs from the set of the three cells that meet at the vertex. The normalization factor $\mathcal{N}^2 = \sum_{(ij)} T_{ij}^2$ is chosen such that $\text{Tr } \mathbb{T} = 1$. The difference of the eigenvalues of \mathbb{T} quantifies the magnitude of tension anisotropy. When the interface angles at the vertex are all identical to 120° the tension anisotropy vanishes. For non-identical vertex angles the tension is locally anisotropic and the dominant eigenvector of \mathbb{T} points along the principal axis of stress. Anisotropic tension also implies that the tension triangle is non-equilateral. The tension triangle's axis of elongation is perpendicular to the principal axis of tension because the tension triangle vectors are rotated by 90° relative to the interfaces (cf. Fig. 2B).

In passing, we note that the tension anisotropy tensor is closely related, but not exactly equal, to the stress tensor σ . Instead it has the form of a metric tensor and thus describes the local geometry of tension space. Specifically, the \mathbb{T} measures the *extrinsic* anisotropy of tension and is complementary to the *intrinsic* shape tensor that we will introduce in the next section.

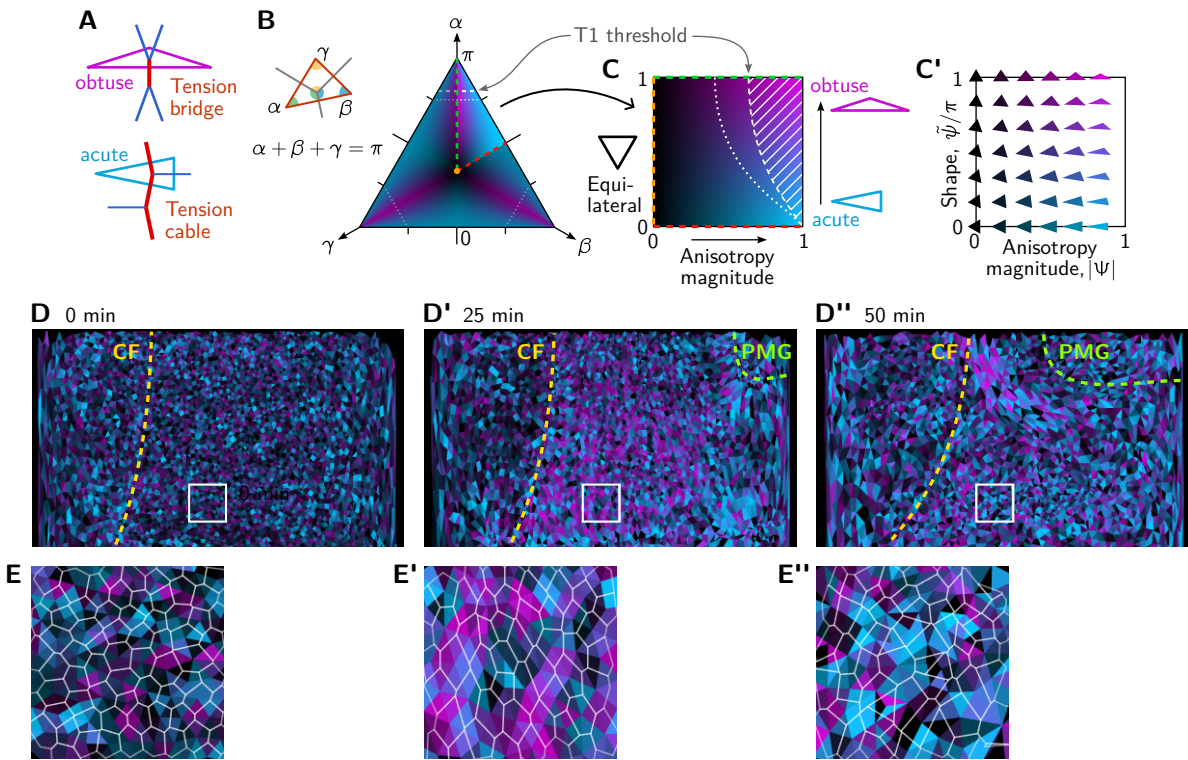


Figure S7: Quantification of local tension configurations (LTC) in terms of tension triangle shape. **A** Tension triangle shape characterizes the local tension configuration. **B** Space of triangles in barycentric coordinates using the angles $\alpha + \beta + \gamma = \pi$. Color indicates the degree of acuteness vs obtuseness by hue from cyan to magenta and the magnitude of anisotropy by brightness (see text for details). A single fundamental domain is highlighted. The remaining shape space is composed of rotated and reflected copies of this fundamental domain, corresponding to permutations of the angles α, β, γ . Dashed white lines indicate the threshold for neighbor exchanges based on the (generalized) Delaunay condition for pairs of identical tension triangles [36]. **C and C'** Triangle shape space spanned by the anisotropy magnitude $|\Psi|$ and acute-vs-obtuse parameter $\tilde{\psi}/\pi$ as axes. See main text for the definitions of Ψ and $\tilde{\psi}$. **D–D''** Snapshots showing the tension configuration at the onset of GBE. For each vertex, a triangle is drawn between the centroids of the adjacent cells and colored according to the tension triangle associated to the vertex. Yellow and green lines marks the cephalic furrow (CF) and the boundary of the posterior midgut (PMG), respectively. **E–E''** Blowups of the white square in (D–D'').

1.7 Local tension configuration

In the main text, we argued that local configuration of tensions at a vertex is characterized by the shape of the tension triangle. Specifically, acute triangles correspond to tension cables, while obtuse triangles correspond to tension bridges (see Fig. S7A).

Whether a triangle is obtuse or acute is an *intrinsic* property, i.e. it is independent of the position, orientation and size of the triangle in the embedding space. The intrinsic shape of a triangle is given by its angles. Since these angles sum to π , we can represent the space of triangle shapes in barycentric coordinates (see Fig. S7B). The center of the barycentric shape space corresponds to an equilateral triangle, while the edges correspond to triangles where one angle is zero and the corners to triangles where two angles are zero. Because the order of labeling the angles in the triangle is arbitrary, the shape space is invariant under permutations of the angles and a single fundamental domain (highlighted in Fig. S7B) is representative.

In the triangle shape space, we have colored each point according to how anisotropic and how acute-vs-obtuse it is. We already know that we can read off

the magnitude of anisotropy from the eigenvalues of the tensor \mathbb{T} , defined in the previous subsection. To quantify the shape (acute vs obtuse), we define a second tensor

$$(\mathcal{S})_{IJ} = \frac{1}{\mathcal{N}^2} \mathbf{T}_I \cdot \mathbf{T}_J, \quad (13)$$

where the indices $I, J \in \{1, 2, 3\}$ are short hand labels for the three interfaces that meet a tri-cellular vertex. Because $\sum_I \mathbf{T}_I = 0$ (force balance), this tensor has the null vector $(1, 1, 1)^T$. To get rid of this nullspace, we go to barycentric coordinates by defining the pair of vectors, $\tau_{1,2}$ that we pack into a matrix

$$\mathfrak{T} = \begin{pmatrix} \tau_1 \\ \tau_2 \end{pmatrix} = \frac{1}{\sqrt{2}\mathcal{N}} \begin{pmatrix} \mathbf{T}_1 - \mathbf{T}_2 \\ \mathbf{T}_3 / \sqrt{3} \end{pmatrix}. \quad (14)$$

These vectors have the defining property that they are orthogonal to one another and to the null vector $(1, 1, 1)^T$ of \mathcal{S} . Now we can define the shape tensor

$$\mathbb{S} = \mathfrak{T} \mathfrak{T}^T = \begin{pmatrix} \|\tau_1\|^2 & \tau_1 \cdot \tau_2 \\ \tau_1 \cdot \tau_2 & \|\tau_2\|^2 \end{pmatrix}. \quad (15)$$

Observe that

$$\mathfrak{T}^T \mathfrak{T} = \tau_1 \otimes \tau_1 + \tau_2 \otimes \tau_2 = \mathbb{T}, \quad (16)$$

which implies that \mathbb{T} and \mathbb{S} share the same eigenvalues. In fact we can perform a singular value decomposition of \mathfrak{T}

$$\mathfrak{T} = R(\psi/2) \Lambda R(-\phi), \quad (17)$$

where $R(\phi)$ is the rotation matrix with angle ϕ and $\Lambda = \text{diag}(\lambda_1, \lambda_2)$ is a diagonal matrix of singular values whose squares λ_1^2, λ_2^2 are the eigenvalues of \mathbb{T} and \mathbb{S} . Because we normalized the tension vectors, $\text{Tr } \mathbb{T} = \text{Tr } \mathbb{S} = \lambda_1^2 + \lambda_2^2 = 1$. ϕ is the angle of the dominant eigenvector in physical space, which gives the orientation of the principal axis of stress. As we will see below, the angle ψ indicates whether the triangle is obtuse or acute. The reasoning to define the rotation based on $\psi/2$ will become apparent below when we represent the shape tensor by a complex number.

The shape tensor \mathbb{S} has only two degrees of freedom, the difference of eigenvalues $\lambda_1^2 - \lambda_2^2$ (which it shares with the tensor \mathbb{T}) and the angle ψ that sets the orientation of its two orthogonal eigenvectors. We can represent \mathbb{S} by a complex number

$$\Psi = \frac{\tau_1^2 - \tau_2^2 + 2i \tau_1 \cdot \tau_2}{\tau_1^2 + \tau_2^2} = |\Psi| e^{i\psi}, \quad (18)$$

where $|\Psi| = |\lambda_1^2 - \lambda_2^2|$ is the magnitude of tension anisotropy and the phase ψ is the “shape space angle” defined by Eq. (17).

Permutations of the edge indices α correspond to sign changes and rotations of ψ by integer multiples of $2\pi/3$. To mod out these group actions (which correspond to the symmetries of the barycentric shape space Fig. S7B), we define

$$\tilde{\psi} = |3\psi \bmod_{\pi} 2\pi| \in [0, \pi], \quad (19)$$

where $x \bmod_d n = (x+d \bmod n) - d \in [-d, n-d]$ is the modulo operation with offset d . This shape parameter informs how acute or obtuse a tension triangle is. For an acute isosceles triangle, $\tilde{\psi} = 0$, whereas for an obtuse isosceles triangle $\tilde{\psi} = \pi$. For non-isosceles triangles, $\tilde{\psi}$ takes values in $[0, \pi]$ quantifying the relative degree of acuteness vs obtuseness. For an equilateral triangle, $|\Psi| = 0$ and $\tilde{\psi}$ is not defined. The axes $|\Psi|$ and $\tilde{\psi}/\pi$ span the space of triangle shapes shown in Fig. S7.

As an alternative to the above mathematical derivation of the shape parameter, we briefly discuss a more intuitive parameter as follows: For a given tension triangle, label its edges in ascending order of length (i.e. T_2 and T_3 will second highest and highest tension, respectively). We can now define a the parameter

$$p = 2 \frac{|T_2 - T_3|}{T_2 + T_3} \in [0, 1], \quad (20)$$

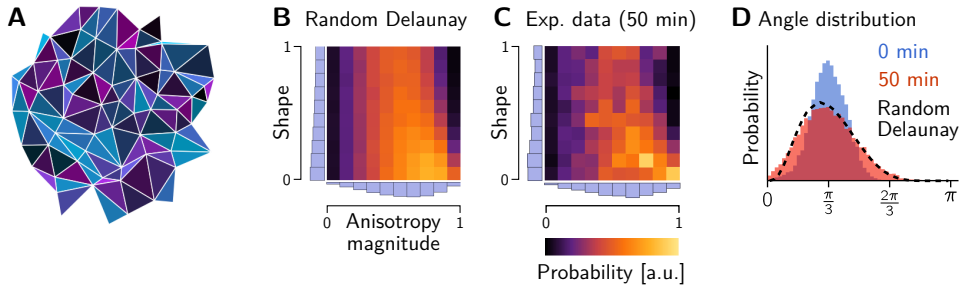


Figure S8: Shape statistics of random a Delaunay triangulation. **A** Example of a random Delaunay triangulation seeded by a Ginibre random point process. Triangles have been colored according to the shape parameters ($|\Psi|, \tilde{\psi}$) (cf. Fig. S7C). **B and C** Histograms showing the triangle shape distribution for the Ginibre-based random Delaunay triangulation (B), tension triangles from the lateral ectoderm at the end of GBE (C, cf. Fig. 7C). **D** Initial and final angle distributions in the lateral ectoderm compared to a random Delaunay triangulation. The initial distribution matches a perturbed equilateral triangular lattice.

which quantifies the relative tension difference between the two largest tensions at a vertex. For a tension cable, there are two large tensions which are similar in magnitude, implying that p is small. For a tension bridge, there is one high tension edge meeting two low tension edges so p will be closer to 1. The maximal value $p = 1$ is reached for $T_1 = T_2 = T_3/2$. Remarkably, to very good approximation $p \approx |\Psi|\tilde{\psi}/\pi$.

Random Delaunay triangulation. As a reference for the triangle shape distributions, we generated random Delaunay triangulations based on the Ginibre random point process [90]. A small sample of such a random triangulation is shown in Fig. S8A. The histograms in the triangle shape space Fig. S8B shows good agreement between the Ginibre-based random Delaunay triangulation and the distribution of tension triangle shapes at the end of GBE. Moreover, the marginalized angle distribution (black dashed line), closely matches the experimentally observed distribution (Fig. S8D).

These findings suggest that the local coordination of cortical tensions is lost during GBE and that the local tension configurations approach a maximally disordered state.

2 Isogonal shear

As discussed in the main text (and further elaborated in Ref. [36]) our simulations show that a non-zero cell-level shear modulus is required for extension via active T1s. Here, we analyze the relation of cell-level and tissue-level shear modulus. Crucially, because of the dominance of cortical tensions, a tissue patch in our model will respond to externally applied forces via an isogonal deformation. We first show that an isogonal deformation can create tissue-scale pure shear (on the level of cell centroid displacement – the transformation of cell vertices is necessarily non-affine to preserve angles). Then we show that these pure shear modes correspond to the response of the tissue to external force by computing the Hessian of our cell elastic energy in the subspace spanned by isogonal deformations, and measure the shear modulus.

To show that isogonal modes can create pure shear, not just dilation/contraction of cells, we make use of the isogonal mode parametrization introduced in Ref. [12]. It assigns an isogonal “potential” Θ_i to each cell, and calculates the cell displacements from the Θ_i and the edge tension vectors. In the following, we will show that a constant gradient in the isogonal potential generates a uniform translation in real

space. By integration, this implies that a quadratic spatial profile of the isogonal potential creates a pure shear.

Let us identify the real space edge unit vectors by the two adjacent cells $\mathbf{e}_{ij} = -\mathbf{e}_{ji}$ and denote the corresponding tensions as T_{ij} . Then the tension vectors $\hat{\mathbf{T}}_{ij} = T_{ij}\hat{\mathbf{e}}_{ij}$ form a triangulation, where $\hat{\mathbf{a}}$ denotes the normal vector to \mathbf{a} , i.e. $\hat{\mathbf{a}} \cdot \mathbf{a} = 0$ and $\|\hat{\mathbf{a}}\| = \|\mathbf{a}\|$.

The isogonal displacement \mathbf{u}_{ijk} of the real space vertices \mathbf{r}_{ijk} (identified by the three adjacent cells) is given by

$$\mathbf{r}_{ijk} \rightarrow \mathbf{r}_{ijk} + \mathbf{u}_{ijk} = \mathbf{r}_{ijk} + \frac{1}{S_{ijk}} [\Theta_i \mathbf{T}_{jk} + (\text{cyc.})] \quad (21)$$

where $S_{ijk} = \hat{\mathbf{T}}_{ij} \cdot \mathbf{T}_{ik}$ is the area of the tension triangle (ijk) .

First, observe that the uniform isogonal mode $\Theta_i = \text{const.}$ has no effect on the vertex positions because

$$\mathbf{T}_{jk} + \mathbf{T}_{ki} + \mathbf{T}_{kj} = 0 \quad (\text{force balance}). \quad (22)$$

Now we aim to show that a constant gradient in Θ_i drives a uniform displacement of the \mathbf{r}_{ijk} . Specifically, by uniform gradient we mean $\Theta_i = \mathbf{t}_i \cdot \mathbf{a}$, i.e. a linear gradient in the tension space (\mathbf{t}_i is the position of the tension triangulation vertex corresponding to cell i , such that $\hat{\mathbf{T}}_{ij} = \mathbf{t}_j - \mathbf{t}_i$). To show that the displacement in real space is uniform, it is enough to show that two adjacent vertices are displaced identically. By induction, this implies that all displacements are identical. It is therefore sufficient to consider a quartet of cells ($i = 1-4$), corresponding to a “kite” in tension space (note that $\hat{\mathbf{a}} \cdot \mathbf{b}$ is identical to the wedge product $\mathbf{a} \wedge \mathbf{b}$.)

Because a constant can be arbitrarily added to all Θ_i , we can set $\Theta_1 = 0$ and thus have $\Theta_i = \hat{\mathbf{T}}_{ij} \cdot \mathbf{a}$ for $i = 2, 3, 4$. The displacements now read

$$\mathbf{u}_{123} = \frac{1}{S_{123}} (\hat{\mathbf{T}}_{12} \cdot \mathbf{a} \mathbf{T}_{31} + \hat{\mathbf{T}}_{13} \cdot \mathbf{a} \mathbf{T}_{12}) \quad (23)$$

$$\mathbf{u}_{134} = \frac{1}{S_{134}} (\hat{\mathbf{T}}_{13} \cdot \mathbf{a} \mathbf{T}_{41} + \hat{\mathbf{T}}_{14} \cdot \mathbf{a} \mathbf{T}_{13}) \quad (24)$$

To show that these displacements are identical, we project them onto two conveniently chosen, linearly independent vectors, namely $\hat{\mathbf{T}}_{12}$ and $\hat{\mathbf{T}}_{13}$. For the latter we find

$$\hat{\mathbf{T}}_{13} \cdot \mathbf{u}_{123} = \frac{1}{S_{123}} \hat{\mathbf{T}}_{13} \cdot \mathbf{a} \hat{\mathbf{T}}_{13} \cdot \mathbf{T}_{12} = -\hat{\mathbf{T}}_{13} \cdot \mathbf{a}, \quad (25)$$

$$\hat{\mathbf{T}}_{13} \cdot \mathbf{u}_{134} = \frac{1}{S_{134}} \hat{\mathbf{T}}_{13} \cdot \mathbf{a} \hat{\mathbf{T}}_{13} \cdot \mathbf{T}_{14} = -\hat{\mathbf{T}}_{13} \cdot \mathbf{a}, \quad (26)$$

where we used that $\hat{\mathbf{T}}_{ij} \cdot \mathbf{T}_{ij} = 0$ and applied the definition of S_{ijk} .

Projecting (23) and (24) onto $\hat{\mathbf{T}}_{12}$ gives

$$\hat{\mathbf{T}}_{12} \cdot \mathbf{u}_{123} = \frac{1}{S_{123}} \hat{\mathbf{T}}_{12} \cdot \mathbf{a} \hat{\mathbf{T}}_{12} \cdot \mathbf{T}_{31} = -\hat{\mathbf{T}}_{12} \cdot \mathbf{a} \quad (27)$$

$$\hat{\mathbf{T}}_{12} \cdot \mathbf{u}_{134} = \frac{1}{S_{134}} (\hat{\mathbf{T}}_{13} \cdot \mathbf{a} \hat{\mathbf{T}}_{12} \cdot \mathbf{T}_{41} + \hat{\mathbf{T}}_{14} \cdot \mathbf{a} \hat{\mathbf{T}}_{12} \cdot \mathbf{T}_{13}) \quad (28)$$

To show equality of these two right-hand sides, we use that given $\hat{\mathbf{T}}_{13} \cdot \mathbf{a}$ and $\hat{\mathbf{T}}_{14} \cdot \mathbf{a}$ we can find \mathbf{a} and substitute the result into $\hat{\mathbf{T}}_{12} \cdot \mathbf{a}$. We start by “expanding the identity”

$$\begin{pmatrix} -\hat{\mathbf{T}}_{13} \\ -\hat{\mathbf{T}}_{14} \end{pmatrix} \mathbf{a} = \begin{pmatrix} \hat{\mathbf{T}}_{13} \cdot \mathbf{a} \\ \hat{\mathbf{T}}_{14} \cdot \mathbf{a} \end{pmatrix} \Rightarrow \mathbf{a} = \begin{pmatrix} -\hat{\mathbf{T}}_{13} \\ -\hat{\mathbf{T}}_{14} \end{pmatrix}^{-1} \begin{pmatrix} \hat{\mathbf{T}}_{13} \cdot \mathbf{a} \\ \hat{\mathbf{T}}_{14} \cdot \mathbf{a} \end{pmatrix} \quad (29)$$

Explicitly writing out the inverse matrix then gives

$$\mathbf{a} = \frac{1}{\hat{\mathbf{T}}_{13} \cdot \mathbf{T}_{14}} \begin{pmatrix} | & | \\ \mathbf{T}_{14} & -\mathbf{T}_{13} \\ | & | \end{pmatrix} \begin{pmatrix} \hat{\mathbf{T}}_{13} \cdot \mathbf{a} \\ \hat{\mathbf{T}}_{14} \cdot \mathbf{a} \end{pmatrix} \quad (30)$$

With this, we find the relation

$$\hat{\mathbf{T}}_{12} \cdot \mathbf{a} = -\frac{1}{S_{134}} (\hat{\mathbf{T}}_{12} \cdot \mathbf{T}_{41} \hat{\mathbf{T}}_{13} \cdot \mathbf{a} + \hat{\mathbf{T}}_{12} \cdot \mathbf{T}_{13} \hat{\mathbf{T}}_{14} \cdot \mathbf{a}) \quad (31)$$

where we used $\mathbf{T}_{ij} = -\mathbf{T}_{jk}$ to flip the indices on \mathbf{T}_{14} . Comparing to (27) and (28) now shows the identity of their RHSs.

Taken together, we have shown that

$$\hat{\mathbf{T}}_{12} \cdot \mathbf{u}_{123} = \hat{\mathbf{T}}_{12} \cdot \mathbf{u}_{134} \quad \text{and} \quad \hat{\mathbf{T}}_{13} \cdot \mathbf{u}_{123} = \hat{\mathbf{T}}_{13} \cdot \mathbf{u}_{134}, \quad (32)$$

Because $\hat{\mathbf{T}}_{12}$ and $\hat{\mathbf{T}}_{13}$ are linearly independent, it follows that $\mathbf{u}_{123} = \mathbf{u}_{134}$. QED.

We just showed that a constant gradient in Θ_i corresponds to a uniform displacement of the real space vertices \mathbf{r}_{ijk} . We can therefore think of $\Theta(\mathbf{t})$ as a “potential” for the isogonal displacement field: $\mathbf{u} \approx \nabla_{\mathbf{t}} \Theta$, where the approximation is valid for slowly varying gradients and exact for constant gradients. The gradient $\nabla_{\mathbf{t}}$ is taken in *tension space* because the function $\Theta(\mathbf{t}_i) = \Theta_i$ is defined on the vertices of the tension triangulation \mathbf{t}_i .

A pure shear aligned with the coordinate axes is given by a displacement field $\mathbf{u}(\mathbf{r}) = \varepsilon \operatorname{diag}(1, -1) \cdot \mathbf{r}$ and is therefore generated (approximately) by a quadratic isogonal potential $\Theta = \varepsilon \mathbf{t}^T \cdot \operatorname{diag}(-1, 1) \cdot \mathbf{t} = \varepsilon [(t^1)^2 - (t^2)^2]$.

3 Simulation methods

In the following, we explain the simulation details for Fig. 4, where we present a model of a single intercalating quartet. The code for the simulations shown is available online: https://github.com/nikolas-clausen/geometric_basis_of_convergent_extension_simulation.

Our model is based on two assumptions: adiabatic force balance, and dominance of cortical tensions. The first assumption means that we obtain the instantaneous cell geometry by solving force-balance equations. The second assumption means the we do so in two steps: first, we determine the interface angles from the cortical tension force balance. The remaining forces in the system are much weaker than cortical tensions and only affect the residual degrees of freedom, the isogonal modes.

In this work, we only consider a symmetric lattice of identical tension triangles, so a number of simplifications occur (the general case of a disordered cell array is the subject of the companion paper [91]). In this case, the cell shape is completely specified by the three vertex angles ϕ_i and edge lengths ℓ_i at each vertex, with $i \in \{0, 1, 2\}$. Because the cell array is a symmetric lattice, the edge lengths ℓ_i can be changed without affecting the angles and therefore parameterize the isogonal degrees of freedom.

We assume that the dynamics of the tensions are determined by a mechano-sensitive feedback loop implementing positive tension feedback. To account for the dynamics of a junction post T1, each junction at a vertex is characterized by the total tensions T_i , and the passive tension $T_{p,i}$. The tensions at a vertex evolve according to:

$$\dot{T}_i = \tau_T^{-1} T_i^n - \tau_p^{-1} T_{p,i} - \frac{1}{3} \sum_k (\tau_T^{-1} T_k^n - \tau_p^{-1} T_{p,k}) \quad (33)$$

where $n > 1$ and τ_T is a time scale converting simulation time into minutes (fit to the data). The passive tension is 0 on all junctions except those that were newly created by a T1 transition. The initial value of T_p on those interfaces is discussed below. Given the tensions, we first calculate the angles from the tensions using the law of sines as $\phi_i = \sin^{-1} \left(\frac{T_i}{2R} \right)$, where R is the tension triangle circumradius.

Cell shape energy To determine the ℓ_i , we minimize the an elastic energy based on the cell shape tensor:

$$S_C = \sum_i \frac{\mathbf{e}_i \otimes \mathbf{e}_i}{\ell_i} \quad (34)$$

where i runs over the edges of the cell \mathcal{C} , and \mathbf{e}_i is the vector pointing from one vertex of the interface to the other. Note that in this shape tensor, each edge contributes linearly in length to the cell shape. This means that artificially subdividing an edge has no effect on the cell shape tensor. This makes sense if we assume that the elasticity we aim to model using S resides in the cell interior (incompressibility, microtubules, intermediate filaments, nucleus). The shape tensor can also be defined using vectors from the cell centroid to its vertices (in the lattice, the two definitions are equivalent). An alternative definition of the elastic energy using $\tilde{S}_C = \sum_i \mathbf{e}_i \otimes \mathbf{e}_i$ instead gives broadly similar results (although interface collapse happens more abruptly, because of the higher order non-linearity).

We assign a reference shape S_0 . An isotropic $S_0 \propto \text{Id}$ favours equilateral hexagons. We chose a slightly anisotropic reference shape S_0 (15% anisotropy) to model the isogonal stretching caused by the ventral furrow before onset of GBE. This anisotropy sets the angle at which the inner interface collapses, $\ell_0 = 0$. The experimental value of the collapse tension was therefore used to fit the S_0 -anisotropy.

We define the cell elastic energy via

$$E_C = \lambda[\text{Tr}(S_C - S_0)]^2 + \mu\text{Tr}[(S_C - S_0)^2] \quad (35)$$

with bulk modulus λ and shear modulus μ . We used a shear/bulk ration of $\mu/\lambda = 0.1$. Because of the separation of scales between cortical tensions and elastic energy baked into the model, the absolute values of λ, μ are irrelevant. Further, for the case of active T1s, the results do not depend on μ/λ , as long as $\mu > 0$.

The edge lengths ℓ_i can now be determined by minimizing the elastic energy Eq. (35) w.r.t. the ℓ_i , for the angles determined by the tension dynamics.

Comparison to area-perimeter elastic energy Strikingly, within the single-quartet model, the “shape strain” $S_C - S_0$ can always be set to 0 by choice of the edge lengths, and the energy $E_C = 0$ throughout. This can already be seen from a degree-of-freedom count (three ℓ_i for the three independent components of $S_C - S_0$). The elastic energy therefore acts only on the isogonal modes (i.e. $\partial_{\phi_i} E_C|_{\ell_i=\text{minimizers}} = 0$) and there is no energy barrier for intercalations. Consequently, there is no need for noise to drive intercalations in our model. By contrast, for the widely-used area-perimeter elastic energy $E = (A - A_0)^2 + (P - P_0)^2$ (where A, P are the cell area and perimeter, and A_0, P_0 their target values) [56], there exists an energy barrier, and the inner interface ℓ_0 only collapses when $\phi_0 = \pi$. This is shown in Fig. S9B. Note that the area-perimeter energy is a special case because of the geometric incompatibility of area and perimeter constraints. Combining area elasticity with shear elasticity based on the shape tensor, $E = (A - A_0)^2 + \mu\text{Tr}[(S_C - S_0)^2]$, (or perimeter elasticity with cell shape bulk elasticity) leads to similar results as Eq. (35). Note also that because of the degree-of-freedom count, the system is under-specified if the shear modulus is 0, foreshadowing the fact that without shear modulus, no convergence-extension takes place [91].

Myosin handover and passive tension. When an interface collapses, $\ell_i = 0$, the tension triangulation is modified topologically: the edge corresponding to the collapsed interfaces is replaced by one corresponding to the new interface (triangulation “flip”). To complete our model, we must specify the initial conditions of this new edge.

As shown in Fig. 4D, we propose a myosin handover mechanism to explain the extension of the new interface post intercalation. A interface with cortical tension T is comprised of the adherens-junctional actomyosin cortex of the two

adjacent cells, which are coupled mechanically via adherens junctions. Under force balance, the total tension T has to be constant along the cortex, but the individual tensions on either side can be non-uniform, as the resulting traction forces are exchanged via adherens junctions. In the following, we assume as a first order approximation that the level of active tension (i.e. myosin concentration) varies linearly along an interface (similar calculations have been performed in Ref. [58] to calculate interfacial shear stress). This allows us to geometrically obtain the myosin concentration at the individual cortices that will form the two juxtaposed sides of the new interface (see Fig 4D).

Consider the tensions T_0, T_1, T_2 at a vertex, and let 0 be the interface about to collapse. The three cells that meet at the vertex will be referred to by (01), (12), (21) (where e.g. (01) is the cell abutting interfaces 0 and 1). Let m_{01}, m_{12}, m_{21} be the motor molecule concentrations (in units of tension) at the vertex in the junctional cortices of the three cells. Then, the tensions are related to the motor molecule concentrations as:

$$T_0 = m_{21} + m_{01}, \quad T_1 = m_{01} + m_{12}, \quad T_2 = m_{12} + m_{21}.$$

This uses the assumption of myosin continuity at vertices, and the fact that the tension on an interface is the sum of the tensions of the two cortices that make it up. The motor molecule concentration on the cortex belonging to the new interfaces, post collapse, will be equal to m_{12} . Solving for this in terms of the tensions:

$$m_{12} = \frac{T_1 + T_2 - T_0}{2}$$

The new interface consists of two cortices, coming from the two vertices of the old junction. Let the tensions at the two triangles be T_0, T_1, T_2 and T_0, T'_1, T'_2 . Let T_a be the active tension on the new junction immediately after the T1. It is the equal to

$$T_a = \frac{(T_1 + T_2 - T_0) + (T'_1 + T'_2 - T_0)}{2} \quad (36)$$

Note however that the total tension T_n on the new junction is not necessarily equal to T_a . The total tension is defined geometrically from the angles at the new junction (or, equivalently, the tension triangle vertices). Indeed, generally, $T_n > T_a$, i.e. the active tension on the new junction is not enough to balance the tension due to the adjacent edges. We introduce a passive tension T_p on the new edge which balances this deficit

$$T_p = T_n - T_a = T_n - (m_{12} + m'_{12})$$

For example, if a perfectly symmetric quartet collapses when the vertex angle facing the collapsing edge is 90° , $T_1 = T_2 = T'_1 = T'_2 = 1$ and $T_0 = T_n = \sqrt{2}$. Therefore, $T_{a,n} = 2 - \sqrt{2} \approx 0.6$ and $T_{p,n} = \sqrt{2} - (2 - \sqrt{2}) \approx 0.8$. Note that by the triangle inequality, for any convex quadrilateral with perimeter P and diagonals D_1, D_2 , one has $P/2 \leq D_1 + D_2 \leq P$. Applying this to the quadrilateral formed by the two tension triangles at the collapsing interface, we get $T_{a,n} \geq 0$ and $T_{p,n} \geq 0$: the handover formula always results in positive active and passive tensions. Further, the “handover” mechanism robustly generates irreversible T1s: if a junction were to collapse back after a T1, the newly formed junction would inherit high myosin levels and therefore be likely to collapse again.

The passive tension subsequently relaxes visco-elastically with rate τ_p^{-1} : $\dot{T}_p = -\tau_p^{-1}T_p$. Combining this with the feedback equation yields Eq. (33). The relaxation rate $\tau_p = \tau_T/6$ was fit to the measured tension decay post intercalation.

Numerical implementation We integrated Eq. (33) using a 4th order Runge-Kutta method as implemented in the SciPy software package [92], using as initial conditions the vertex angles in the experimental data at time $t = 5$ min (the vertex

angles from the data were temporally smoothed with a window of 2 min to reduce noise).

In our simulations, we triggered an intercalation event once the collapsing edge length, as determined by energy minimization, reached 0. We then initialized the passive tension as given by Eq. (36) and simulated the combined active/passive tension dynamics. The overall time- and length-scale were likewise fit to the data. The feedback exponent was $n = 4$. Numerically, energy minimization was carried out using the `scipy.optimize` package, specifically its Nelder-Mead optimizer.

Passive intercalation. Within the same framework, we can also model passive intercalations, shown in Fig. 4F. We can either specify cortical tension dynamics (in this case, tension homeostasis, $\dot{T} \sim -(T - 1)$) and then minimize an elastic energy that includes the influence of externally imposed shear. This will trivially reproduce the isogonal behavior shown in Fig. 2E. Alternatively one can reason that on the dorsal side there is very little active tension (cortical myosin), so that cortical tensions are expected to be low. Then, the passive elastic energy, together with the imposed shear, should determine the also angles. Both models are consistent with the data.

In Fig. 4F, we show simulations based on the latter option. We implement the externally imposed shear causing the passive intercalations as follows. We calculate the four cell centroids \mathbf{c}_i of the cell quartets, and demand that at simulation time t

$$\mathbf{c}_i(t) = S(t) \cdot \mathbf{c}_i(t = 0) \quad (37)$$

where $S(t)$ is a diagonal matrix representing (area-preserving) shear, increasing over time with constant shear rate γ .

We then minimize the elastic energy under the constraint (numerically, this is done by adding a penalty term to the elastic energy), but this time with respect to both the lengths ℓ_i and the angles ϕ_i . As long as the shear modulus $\mu \ll \lambda$, this procedure results in approximately isogonal behavior. We chose $\mu = 0.01\lambda$. To obtain continuity across the intercalation, the rest shape S_0 needs to be adjusted. Otherwise, post intercalation, the cell quartet jumps back to a hexagonal lattice configuration. This can be done by introducing a viscous relaxation scale for the rest shape; for simplicity, we simply set the rest shape to the current shape tensor at the time of intercalation. The initial conditions are obtained by varying the angle between the shear axis and the collapsing interface orientation from $0^\circ - 25^\circ$.

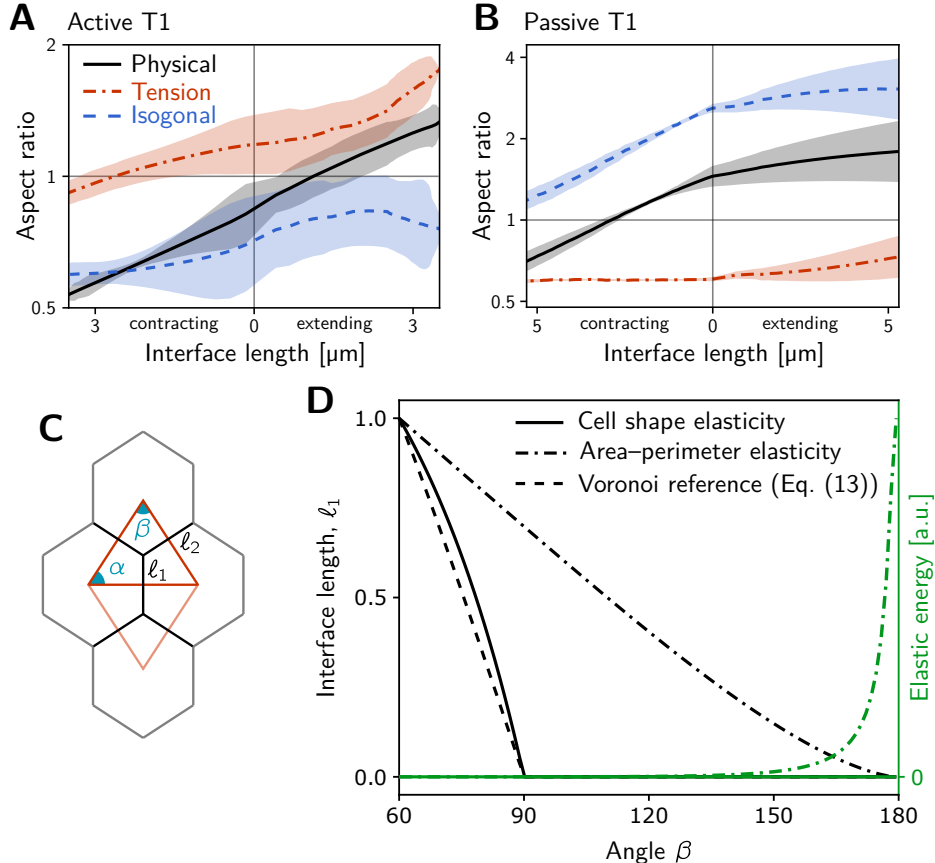


Figure S9: Additional quantification of single-quartet simulations. **A and B** Tension-isogonal decomposition of cell quartet shape during active (A) and passive (B) T1s in the single-quartet model (same simulations as Fig. 4E–F). **C** Geometry of a quartet of identical cells and the corresponding tension triangles (red) parametrized by the angles α, β . **D** Comparison of different cell shape elastic energies which determine the cell interface lengths ℓ_i as a function of the angles α, β . The plot shows the inner interface length for a left-right symmetric quartet (i.e. an isosceles tension triangle) where $\alpha = (\pi - \beta)/2$. For reference, the inner interface length ℓ_{ref} for a Voronoi tessellation based on the tension triangles is shown (dashed black line). The interface length obtained by minimizing elastic energy Eq. (3) with isotropic target shape (solid black line) closely follows the reference Voronoi length and vanishes at the same critical angle. By contrast, minimizing the “area-perimeter” energy of the vertex-model $E_{\text{cell}} \sim (A - A_0)^2 + (P - P_0)^2$ gives a interface length (dot-dashed black line) that vanishes only for $\beta \rightarrow \pi$ and the elastic energy diverges in this limit (dashed green line). This implies that tension dynamics, changing the angles at vertices, cannot drive T1s for this choice of elastic energy in the absence of noise.

4 Movie captions

Movie 1: Side view and flat projection of one side of the embryo surface. Ventral furrow invagination (gray cells on the dorsal side) is followed by convergence-extension of the germ band (lateral ectoderm cells colored purple, blue and green). As the germ band elongates along the AP axis, the cells move over the posterior pole. The amnioserosa (orange and red cells) undergoes convergence-extension in the opposite direction of the germ band and exhibits significant cell shape elongation while cells in the germ band remain mostly isotropic in shape. Near the end of germ band extension (ca 35 min) cell divisions start. (Corresponds to Fig. 1A; invaginating cells are colored in gray; cells in the head are colored white; cells after division events are colored in light gray.)

Movie 2: Relative tension dynamics in the lateral ectoderm. Relative junctional tensions inferred from cell geometry reveals show the emergence of an alternating pattern of high and low tensions that organizes cell intercalations (T1 transitions). Coherent intercalations drive convergent-extension tissue flow which slows down significantly as cell scale order is lost.

Movie 3: Simulation of single intercalating cell quartet. Simulation of an intercalating cell quartet driven by positive tension feedback and myosin handover mechanism, corresponding to Fig. 4E. Out of the ensemble from Fig. 4E, the movie and shows a simulation for symmetric initial tensions (i.e. equal initial tensions on the two non-collapsing interfaces $T_1 = T_2$). After the edge flip, the blue parts of the inner tension triangulation edge indicate the passive tension on the newly formed interface. The passive tension rapidly relaxes while the active tension grows due to positive tension feedback.